10.1098/rspa.2000.0702

THE ROYAL SOCIETY

A laboratory study of the focusing of transient and directionally spread surface water waves

By T. B. Johannessen† and C. Swan

Department of Civil and Environmental Engineering, Imperial College of Science, Technology and Medicine, London SW7 2BU, UK

Received 24 February 2000; revised 22 August 2000; accepted 7 September 2000

This paper describes a new laboratory study in which a large number of waves, of varying frequency and propagating in different directions, were focused at one point in space and time to produce a large transient wave group. A focusing event of this type is believed to be representative of the evolution of an extreme ocean wave in deep water. Measurements of the water-surface elevation and the underlying water-particle kinematics are compared with both a linear solution and a second-order solution based on the sum of the interactions first identified by Longuet-Higgins & Stewart. Comparisons between these data confirm that the directionality of the wavefield has a profound effect upon the nonlinearity of a large wave event. If the sum of the wave amplitudes generated at the wave paddles is held constant, an increase in the directional spread of the wavefield leads to lower maximum crest elevations. Conversely, if the generated wave amplitudes are increased until the onset of wave breaking, at or near the focal position, an increase in the directional spread allows larger limiting waves to evolve.

An explanation of these results lies in the redistribution of the wave energy within the frequency domain. In the most nonlinear wave cases, neither the water-surface elevation nor the water-particle kinematics can be explained in terms of the free waves generated at the wave paddles and their associated bound waves. Indeed, the laboratory data suggest that there is a rapid widening of the free-wave regime in the vicinity of a large wave event. For a constant input-amplitude sum, these important spectral changes are shown to be strongly dependent upon the directionality of the wavefield. These findings explain the very large water-surface elevations recorded in previous unidirectional wave studies and the apparent contrast between unidirectional results and recent field data in which large directionally spread waves were shown to be much less nonlinear. The present study clearly demonstrates the need to incorporate the directionality of a wavefield if extreme ocean waves are to be accurately modelled and their physical characteristics explained.

Keywords: focused waves; nonlinear waves; wave groups; wave nonlinearity; directional waves

† Present address: Kværner Oil and Gas a.s., PO Box 222, N-1326 Lysaker, Norway.

1. Introduction

In an earlier paper, Baldock *et al*. (1996), hereafter referred to as BST, describe a laboratory study of nonlinear surface water waves undertaken in a two-dimensional wave flume. Within this study they focused a large number of wave components, of varying frequency, at one point in space and time to produce a large transient wave group. Measurements of the water-surface elevation and the underlying water-particle kinematics were compared with both a linear wave theory and a second-order solution based on the sum of the wave–wave interactions first identified by Longuet-Higgins & Stewart (1960). The laboratory data confirmed that the nonlinear wave–wave interactions produce a highly nonlinear wave group in which the central wave crest is higher and narrower than either the linear or the second-order solution, while the adjacent wave troughs are broader and less deep. For example, if one considers the most nonlinear wave group observed by BST (case D55 in figure 6*c*, p. 660), the maximum measured crest elevation was more than 40% larger than that predicted by the linear sum of the underlying free waves generated at the wave paddle. Furthermore, the measured data were also more than 30% larger than the predicted second-order solution.

These results suggest that the formation of a focused wave group involves significant transfers of energy, to both the higher and the lower harmonics, leading to large local increases in the energy density. Although such changes were anticipated, particularly in light of the numerical calculations undertaken by Longuet-Higgins (1987) and the experimental observations of Miller *et al*. (1991), the magnitude of the energy transfers were perhaps surprising and appeared to be at odds with recent field data. For example, Jonathan *et al*. (1994) report on an analysis of field data recorded at the Tern platform in the northern North Sea. Although this dataset includes some of the largest waves ever recorded ($H_{\max} = 26.5$ m and $\eta_{\max} = 17.5$ m, where H is the wave height and $\eta_{\max}$ the crest elevation), the largest individual events appear to be in reasonable agreement with a second-order solution based upon the underlying frequency spectrum. As such, they are clearly less nonlinear than the focused waves recorded by BST.

Although there are several possible explanations for this apparent difference between laboratory and field data, one should not lose sight of the fact that real seas are multi-directional and consequently individual wave events will exhibit some degree of short-crestedness. This is in marked contrast to the flume experiments reported by BST that were unidirectional. The present paper will consider the influence of directionality on the evolution of large waves and will seek to establish if this accounts for the reduced nonlinearity observed in recent field data. To this end, a new series of laboratory observations will be presented in which large isolated wave groups, with varying directional spread, were generated in a laboratory wave basin. Section 2 commences with a brief review of the physical processes and modelling procedures appropriate to the description of large ocean waves. The practical importance of these events is also noted. The experimental apparatus and instrumentation are described in § 3. Section 4 outlines the method of wave generation and describes some preliminary calculations and observations necessary to ensure the validity of the resulting data. The experimental observations are discussed in § 5. These results concern a wide variety of focused wave groups with both varying spectral bandwidth (or frequency distribution) and directional spread. In each case, the intensity of the wave group ranges from near-linear to the limit of incipient wave breaking. Comparisons between these data and both linear and nonlinear wave theories highlight the importance of the directional spread. Section 6 provides some closing remarks and outlines the practical implications of the experimental results.

2. Background

It is now widely recognized that the largest ocean waves do not form part of a regular wave train but occur as isolated events within a random or irregular sea, which rapidly disperse in both space and time. The description of such waves has been the subject of a sustained research effort. This interest arises because they form an important part of the oceanographic environment, and because their description defines the design criteria appropriate to many aspects of both offshore and coastal engineering. In deep water, the occurrence of large waves is believed to be due to the focusing of wave components whereby individual wave crests come into phase at one point in space and time. The statistics of extreme waves were first investigated by Longuet-Higgins (1952), while the effects of finite bandwidth and nonlinearity were clarified at a later date (Longuet-Higgins 1980).

More recently, the inefficiency of long time-domain simulations necessary to provide deterministic representations of irregular wavefields has led to considerable interest in the extremal statistics of a Gaussian wavefield. In particular, much interest has focused on the average shape of an extreme event given the underlying frequency spectra and the crest elevation. Lindgren (1970) first solved this problem in a general context, while Boccotti (1983) applied this representation to ocean waves and showed that the autocovariance function of the wave spectrum yields the mean shape of an extreme event in a Gaussian wavefield (provided the extreme event is large). The autocovariance function also forms the basis of the 'NewWave' design formulation proposed by Tromans *et al*. (1991), and has subsequently been validated against field measurements (Jonathan *et al*. 1994). After correcting for second-order effects, the 'NewWave' model provides a remarkably accurate representation of the mean shape of an extreme wave, provided the crest height is larger than approximately three times the standard deviation of the recorded water-surface elevation. In a further and significant step forward, Phillips *et al*. (1993*a*, *b*) showed that the three-dimensional autocovariance function also defines the limiting shape of an extreme crest in a directional wavefield.

Formulations that describe the mean shape of a wave profile in the vicinity of an extreme crest will necessarily yield a single large event that tapers away either side of the large crest. Far from this crest the wave profile will tend to the mean water level as the phase correlation, present at the large crest, disappears. The wave profile will also be horizontally symmetric about the large crest. In laboratory studies, an extreme event of this type is commonly referred to as a focused wave group. These are produced by simultaneously generating a large number of freely propagating wave components of differing frequency. Their relative phasing is predetermined such that a single large wave group evolves. Having achieved a global maximum crest height, the group disperses. Focused wave groups include both the transient and the nonlinear behaviour of a wavefield and, as will be shown below, they may also incorporate the directional spread. However, they neglect the randomness of an ocean event.

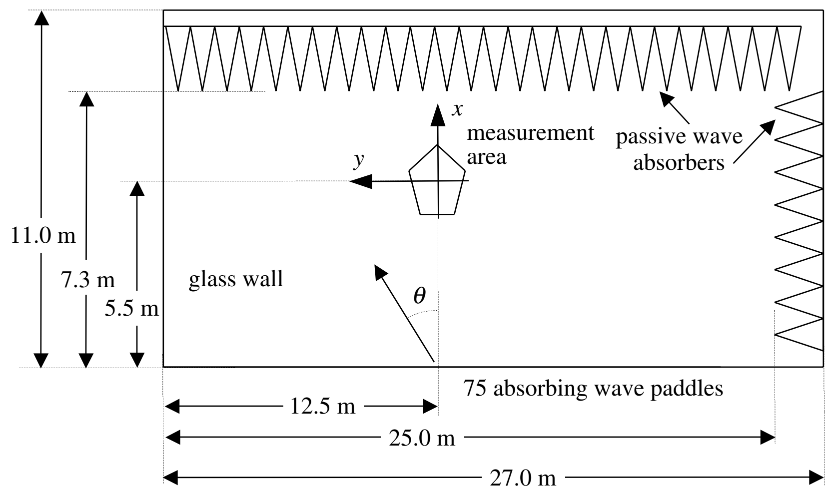

Figure 1. Layout of wave basin.

If one compares the deviations from linear theory observed in laboratory studies with those present in field data, it is clear that the nonlinearity observed in full-scale measurements is considerably weaker than that observed in two-dimensional laboratory data. Compare, for example, field measurements due to Sand *et al*. (1990) and Jonathan *et al*. (1994) with the laboratory observations of Stansberg (1991, 1994) and those provided by BST. Indeed, after correcting for weakly nonlinear second-order effects, Jonathan *et al*. (1994) suggest that both the crest and the trough of even the largest events are very nearly Rayleigh distributed. This is inconsistent with the large deviations from linear and second-order theory observed by BST. Although the frequency spectra investigated within the laboratory studies are necessarily different from the spectra that govern the formation of a large ocean event, the most likely explanation for the observed difference lies in the directional characteristics of an ocean wavefield. Nonlinearity is largely related to the local steepness of a wave profile, and wavefield directionality affects the local steepness even in a linear approximation.

3. Experimental apparatus

(*a*) *Wave basin*

Figure 1 provides a schematic of the wave basin in which the present study was undertaken. This facility, which is located at Edinburgh University, has a plan area of $25\,\mathrm{m} \times 11\,\mathrm{m}$ and supports a constant working depth of 1.2 m. The waves are generated by 75 numerically controlled wave paddles located along one of the longer sides of the wave basin. Each paddle is 0.3 m wide and is bottom-hinged at an elevation of 0.5 m beneath the still water level. The hydrostatic load acting on each paddle is supported mechanically by a system of springs and pulleys, while the drive motor is connected to the paddle via a force transducer. This arrangement allows the simultaneous generation of the desired wave conditions and the active absorption of any reflected wave components. Further details concerning the mechanics of the wave generators and the feedback algorithm are outlined by Salter (1984).

At the downstream end of the wave basin, a large bank of passive absorbers dissipates the incident wave energy. Each absorber consists of a triangular wedge, with the leading face having an included angle of 30° (figure 1). These wedges are formed from galvanized mesh and packed with Expiate, which is expanded aluminium foil having a ragged shape and a large surface area. Passive absorbers of this type are permeable to incident waves propagating in almost any direction (see § 4 *d* below) and provide an effective means of dissipating the majority of the wave energy. Nevertheless, given the difficulties which wave reflections pose in all wave basins, it was also considered prudent to include additional passive absorbers along one of the shorter sides of the wave basin (figure 1). Indeed, the only side that remains unprotected, as far as reflections are concerned, comprises glass panels necessary for visual observations. The influence of this side wall and the effectiveness of the passive absorbers will be considered further in § 4.

Within the present study all the quantitative measurements, including those appropriate to the calibration process, were undertaken within the pentagonal measurement area indicated on figure 1. This was constructed from a rigid steel frame and supported on two stiff steel trusses spanning the short length of the wave basin. Within the measurement area, locating holes, at 100 mm centres, allowed the instrumentation to be positioned with an accuracy of ±2 mm in the (x, y)-directions.

(*b*) *Instrumentation*

Throughout the test programme the water-surface elevations were recorded using surface-piercing resistance wave gauges. Each gauge consists of two vertical stainless steel wires, 2.5 mm in diameter, spaced 12.5 mm apart and supported within a vertical traverse. Previous measurements (see BST) confirm that these wave gauges cause virtually no disturbance of the incident wavefield and provide a voltage output that is directly proportional to their depth of immersion. After direct calibration, undertaken in still water, each gauge provides a time-history of the water-surface elevation, $\eta(t)$, at one spatial position (x, y). Given the purpose of the present tests, to investigate large directionally spread surface waves, a large number of point measurements were required. To prevent interference between individual wave gauges, they were energized at different input frequencies and their minimum spacing set at 100 mm. In any one test, a maximum of 12 wave gauges were located within the measurement area, with repeated runs used to provide the required spatial definition.

Preliminary measurements undertaken within the wave basin identified significant errors associated with a low-frequency drifting of the wave gauge output. The cause of this was eventually found to be relatively small temperature gradients established within the water column when the wave basin was not in use. To overcome this problem, pumps were used to circulate the water, overnight, thereby reducing the temperature variation to less than 0.1 °C. In addition, all wave gauges were calibrated at least twice daily and the data abandoned if significant drifting ($\Delta\eta > 1$ mm) was identified. With these precautions in place, and with the output from the wave gauges low-pass filtered at 25 Hz to remove unwanted noise, the accuracy of the wave gauges was estimated to be ±1 mm.

In addition to the surface elevation data, the horizontal component (x-direction) of the wave-induced orbital velocity was recorded using laser Doppler anemometry

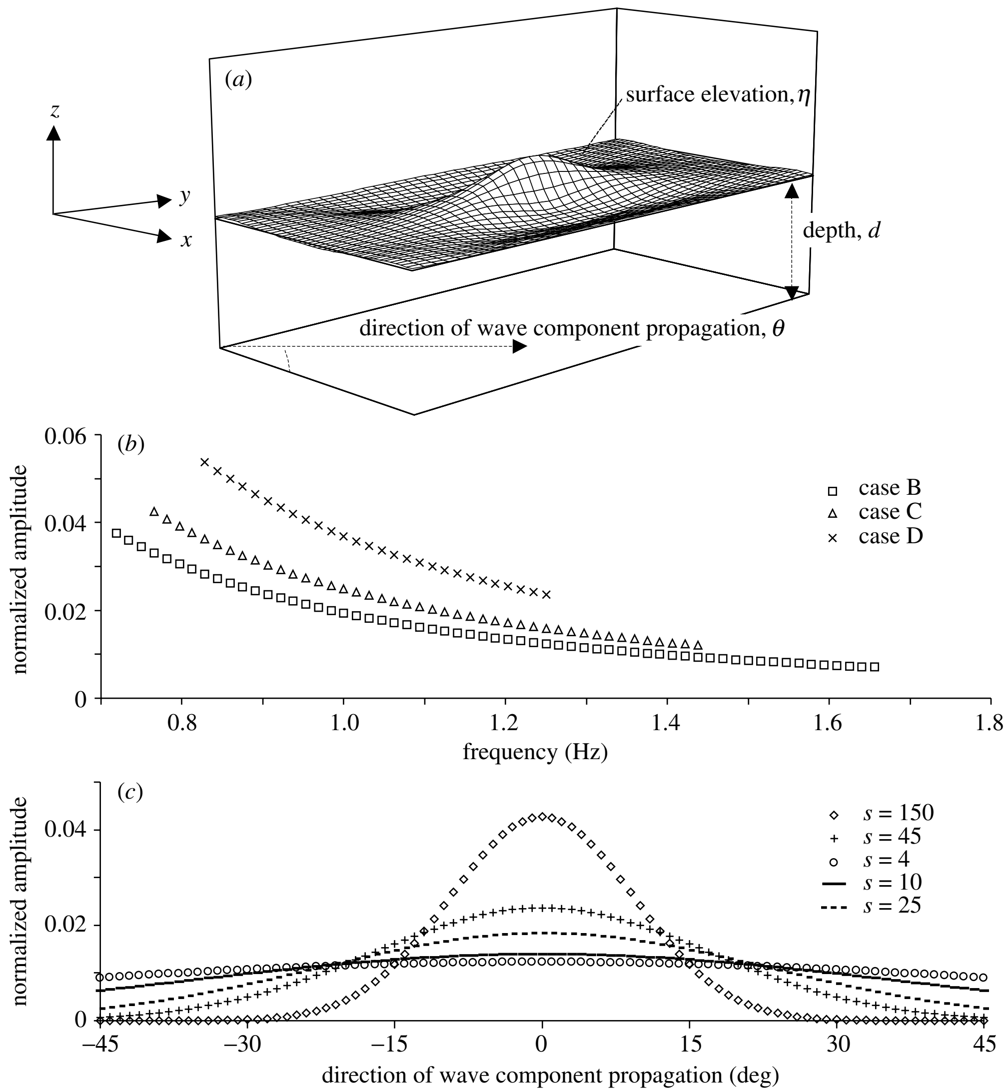

Figure 2. (*a*) Definition sketch. (*b*) Frequency–amplitude spectra $a(\omega)$. (*c*) Directional–amplitude spectra $a(\theta)$.

(LDA). A 35 mW helium–neon laser produced a single beam that was split and phase-shifted using a traditional Bragg cell, and passed down a fibre-optic cable. At the other end of this cable the laser beams were 'launched' through the laser head, the final component of which is a 50 mm converging lens. This laser head is cylindrical in shape, having an external diameter of 12 mm and an overall length of 120 mm. The measuring position, located at the intersection of the laser beams (50 mm downstream of the laser head) was estimated to have a volume of 0.5 mm^3. Given the limited visual access within the wave basin, and the need to keep the measuring position away from the side walls, the anemometer was operated in a back-scatter mode. Accordingly, the receiving camera necessary to record the Doppler bursts containing the velocity data was built into the laser head. Although this method gives a reduced signal-to-noise ratio, relative to a forward-scatter arrangement, it has the key advantage that only the laser head and its supporting traverse were located in the flow field.

Within the present study the successful measurement of the water-particle kinematics beneath the position of the maximum wave crest proved extremely difficult. In particular, measurements within the crest-trough regime, close to the instantaneous water surface, were complicated by the fact that the measuring position was only submerged for a small fraction of a second. The difficulties associated with these measurements were two-fold. Firstly, in those cases involving highly nonlinear wave groups (see § 4 below), the mass transport in the vicinity of the largest wave crest was very large. As a result, it was difficult to achieve the seeding of the flow necessary for the optimal performance of the LDA. To overcome this problem the seeding material (Timiron Supersilk) was first diluted in water to a concentration of *ca.* 600 ppm (by volume) and discharged through five hypodermic needles located *ca.* 1 m upstream of the measurement position. The seeding material was discharged continuously at a rate of *ca.* $1\,\mathrm{l\,min^{-1}}$, just beneath the level of the lowest wave trough and was heated to give a small positive buoyancy so that the seeding remained close to the instantaneous water surface.

The second difficulty concerned the curvature of the free surface. In the short-crested wave groups, the water surface has significant curvature perpendicular to the mean wave direction. With the long axis of the laser head orientated on the plane $x = \text{const.}$, the laser head was submerged for a shorter period than the measuring position, and the signal potentially disrupted by reflections of the laser beams from the water surface on the far side of the wave crest. Once again, the maintenance of an optimal seeding density (*ca.* 100 ppm at the measuring position) was the key to overcoming this difficulty. After numerous trial-and-error adjustments, reliable velocity data were recorded to within 5 mm of the maximum crest elevation. Furthermore, initial tests confirmed that the introduction of the seeding material, the laser head or its supporting traverse did not cause significant disturbance of the flow field at the measurement position. With the flow appropriately seeded, the horizontal component of the wave-induced water-particle kinematics could be measured with an accuracy of $\pm 2\%$. The positional accuracy of the measuring position being estimated to be ± 1 mm in the vertical direction (z) and ± 2 mm in the horizontal directions (x, y).

4. Experimental method

(*a*) *Wave generation*

To create the desired focused wave groups within the laboratory basin, a specified range of wave components, having the required spread in both frequency and direction, were generated and their relative phasing predetermined so that constructive interference occurs at one point in space and time. Longuet-Higgins (1974) was the first to apply this approach in a two-dimensional wave flume. In his study he introduced a continuous modulation of the driving frequency sent to the wave paddle, and thereby created a single breaking event within the wave flume. More recently, Rapp & Melville (1990) and BST applied a linear wave theory to determine the appropriate phasing of unidirectional wave components. In the present study, this latter approach has been adopted and the effects of directional spreading included. Figure 2*a* provides a schematic representation of a linearly focused wave group, where the focus position occurs at $x = y = 0$, $\eta(x, y, t)$ defines the surface elevation, d defines the water depth and θ the direction of wave component propagation. A linear representation of this group is given by:

$$\eta(x, y, t) = \sum_{n=1}^{N} a_n \sum_{m=1}^{M} b_{nm} \cos(k_n(x \cos(\theta_m) + y \sin(\theta_m)) - \omega_n t), \tag{4.1}$$

where a_n defines the amplitude of the nth frequency component, ω_n is its angular frequency (or $2\pi/T_n$, where T_n is the corresponding wave period) and k_n the wavenumber (or $2\pi/\lambda_n$, where λ_n is the wavelength). In accordance with linear theory, ω_n and k_n satisfy

$$\omega_n^2 = g k_n \tanh(k_n d), \tag{4.2}$$

where g is the gravitational acceleration. The directional spread of the wave components, $b(\omega, \theta)$, is normalized so that

$$\sum_{m=1}^{M} b_{nm} = 1, \tag{4.3}$$

and consequently

$$A = \sum_{n=1}^{N} a_n \sum_{m=1}^{M} b_{nm} = \sum_{n=1}^{N} a_n, \tag{4.4}$$

where A represents the linear-amplitude sum and hence the linear crest elevation at the focal position. Within the present investigation it was decided that the directional spread should be independent of the wave frequency $b(\omega, \theta) = b(\theta)$. This enables a systematic investigation of the effects of directionality on the nonlinear behaviour of a focused wave group. It also implies that, in a linear analysis of the surface elevation, $\eta(t)$, recorded at the focal position ($x = y = 0$), is independent of $b(\theta)$. Adopting a typical spreading parameter,

$$b(\theta) = B \cos^s(\tfrac{1}{2}\theta), \tag{4.5}$$

where B is a normalizing coefficient and, for experimental reasons, θ lies in the range $-\frac{1}{4}\pi \leqslant \theta \leqslant \frac{1}{4}\pi$. Equation (4.5) defines a wavefield that is symmetric about the x-axis and has a mean wave direction aligned with this axis.

To facilitate comparisons with the data presented by BST, the present investigation has considered three of the four frequency–amplitude spectra investigated in the earlier study. Adopting identical notation to that used by BST, these spectra are denoted by B, C and D, where B is broad-banded, D is narrow-banded and C is intermediate. Details of each of these spectra are given in table 1*a*, and reproduced in non-dimensional form in figure 2*b*. In each case, $a(\omega)$ decays according to ω^{-2} between the truncation frequencies. All wave groups are periodic in time with a fundamental period of 64 s. The number of non-zero frequency components, N in (4.1), varies with the frequency spectral bandwidth with $N = 61$ in case B, $N = 44$ in case C, and $N = 28$ in case D. Table 1*b* defines the directional–amplitude spectra that, with the exception of the unidirectional case, are classified according to the spreading parameter s. In total, six directional distributions were applied to each of

Table 1. (*a*) *Frequency spectra*

frequency spectrum	spectral shape	frequency range (Hz)	spectral repeat period (s)
B	$a \propto f^{-2}$	$\frac{46}{64} \leqslant f \leqslant \frac{106}{64}$	64
C	$a \propto f^{-2}$	$\frac{49}{64} \leqslant f \leqslant \frac{92}{64}$	64
D	$a \propto f^{-2}$	$\frac{53}{64} \leqslant f \leqslant \frac{80}{64}$	64

Table 1. (*b*) *Directional spectra*

(F is the in-line velocity reduction factor discussed below.)

directional spectrum	spreading parameter	directional range (deg)	F
UD	$s = \infty$ (unidirectional)	$-45 \leqslant \theta \leqslant 45$	1.000
150	$s = 150$	$-45 \leqslant \theta \leqslant 45$	0.987
45	$s = 45$	$-45 \leqslant \theta \leqslant 45$	0.960
25	$s = 25$	$-45 \leqslant \theta \leqslant 45$	0.941
10	$s = 10$	$-45 \leqslant \theta \leqslant 45$	0.918
4	$s = 4$	$-45 \leqslant \theta \leqslant 45$	0.907

the frequency spectra (B, C and D). These include unidirectional events (consistent with the data presented by BST), long-crested events with a small directional spread ($s = 150$) and very-short-crested events with large directional spread ($s = 4$). Four intermediate cases are also considered. In each case, the directional–amplitude spectra were generated with 91 components per frequency ($M = 91$ in (4.1)), spaced at $1°$ intervals. A graphical representation of the directional–amplitude spectra is given in figure 2*c*. For each combination of the frequency and directional spectra, a range of input amplitudes, expressed in terms of the linear-amplitude sum A, are considered. In total, this involves the investigation of 84 different wave groups, full details of which are given in table 2. In each case, $A = 20$ mm corresponds to a near-linear condition, while the largest amplitude used in each of the 18 spectral shapes is within 1 mm of the limit at which wave breaking was first observed.

To distinguish between the large number of test cases, individual wave groups are referred to by the code for the frequency spectrum, the code for the directional spectrum and the linear-amplitude sum in mm. Case D0493 is thus the wave group with frequency spectrum D, a directional spread of $s = 4$ and an input-amplitude sum of $A = 93$ mm. Within table 2 the asterisks denote those cases in which the x components of the water-particle kinematics $u(t)$ were recorded at a large number of closely spaced vertical positions beneath the observed position of the maximum wave crest. For each of these cases, the water-surface elevation corresponding to the so-called 'inverse' wave group was also recorded. These inverse groups are identical to those discussed above, except that the amplitudes of the component waves (a_n in (4.1)) are specified as being negative, thereby creating a group which consists of a large wave trough rather than a large wave crest. The significance of these results will be discussed in § 5.

The test cases indicated in table 2 were chosen to be compatible with the unidirectional data presented by BST. Field data analysed by Jonathan & Taylor (1995)

Table 2. *Experimental test cases*

(* indicates those cases where the x-component of the water particle kinematics were recorded.)

frequency–amplitude spectrum	directional–amplitude spectrum	input-amplitude sum A (mm)
B	$s = \infty$ (unidirectional)	20, 40, 52*
	$s = 150$	20, 40, 55, 59
	$s = 45$	20, 40, 55, 66*
	$s = 25$	20, 40, 55, 70, 71
	$s = 10$	20, 40, 55, 70, 76
	$s = 4$	20*, 40*, 55*, 70*, 78*
C	$s = \infty$ (unidirectional)	20, 40, 55
	$s = 150$	20, 40, 55, 63
	$s = 45$	20, 40, 55, 70, 71
	$s = 25$	20, 40, 55, 70, 76
	$s = 10$	20, 40, 55, 70, 81
	$s = 4$	20, 40, 55, 70, 84
D	$s = \infty$ (unidirectional)	20, 40, 55, 61*
	$s = 150$	20, 40, 55, 70, 71
	$s = 45$	20, 40, 55, 70, 78*
	$s = 25$	20, 40, 55, 70, 85
	$s = 10$	20, 40, 55, 70, 85, 88
	$s = 4$	20*, 40*, 55*, 70*, 85*, 93*

suggest that the directional spread observed in a large North Sea storm may be approximated by a normal distribution with a standard deviation of 30°. This corresponds closely to a value of $s = 7$. However, it is clear that the main difficulty in creating wave groups that are representative of ocean wavefields lies in the necessity of truncating the experimental spectrum in both the directional and the frequency domains. The authors are therefore content with generating focused wave groups with the widest possible range of bandwidths, in both the frequency and the directional domains, and believe that effects which are relevant to an ocean wavefield may be identified.

(*b*) *Calibration*

In contrast to the relatively straightforward and well-documented procedure for calibrating a unidirectional wave flume, the calibration and validation of a directional wave basin by traditional means is a Herculean task. Given the purpose of the present tests, it was critically important to know the amplitude, frequency, phasing and direction of propagation of the individual wave components generated at the wave paddles. Without this information, it would be impossible to quantify the nonlinear interactions arising during the evolution of a focused wave group. This approach is, however, at odds with the common usage of a directional wave basin. This typically involves the generation of some target wave spectrum at a single measurement position and is therefore more interested in the wave characteristics at this point than those generated at the wave paddles. Given the notorious difficulty of controlling wave reflections within a large wave basin, an iterative procedure may produce a reasonable approximation to the target frequency spectrum, but the spatial variability will be large (amplitude variations of 15% are not uncommon) and the direction of propagation of the component waves uncertain.

To achieve the necessary calibration, a first estimate of the transfer function $T(a, \omega, \theta)$ was achieved using regular waves. This function describes the relationship between the numerically generated input signal and the resulting surface elevations. Five frequency components were considered, equally spaced within the frequency range defining case B in table 1*a*. These were combined with nine component directions ($-40° \leqslant \theta \leqslant +40°$ in 10° intervals) and six wave-amplitude sums to give 270 test conditions. In each case, the water-surface elevation was sampled at 12 spatial locations. Although this involves a large amount of work, the resulting calibration was too coarse to provide an accurate definition of the required wave groups and showed considerable spatial variation. For example, although the root-mean-square (RMS) variation in the measured wave amplitude at any one location was less than 2%, variations between different spatial locations were found to be as large as 14%.

To overcome these difficulties, an alternative calibration, based on focused or near-focused wave groups, was established. If it is assumed that a wavefield is linear and unidirectional, equation (4.2) defines the unique relationship between the component wave frequency and wavenumber. Furthermore, if it is also assumed that the wavefield has a repeat period and that measured data are available for the entire period, a standard Fourier transform will resolve the wavefield uniquely, even if measurements are only made at one spatial position. This approach has two significant advantages. Firstly, because the wave groups contain a large number of wave components, they disperse rapidly either side of the focus position. As a result, the waves generated at the wave paddles are small, thereby limiting the difficulties associated with nonlinear wave generation (Schaffer 1993). More importantly, the waves present at both the end wall and the sides of the basin will also be small. Accordingly, the effects of reflections in the vicinity of the measurement area will be much reduced and were, in fact, shown to be negligible. This point is further considered in § 4 *d* below. Secondly, this approach yields information similar to the regular wave calibration, but allows a large number of discrete frequency components to be investigated for each test run. A higher calibration density can therefore be achieved. Within the present study, a broad-banded spectrum (slightly wider than test case B in table 1*a*) was used for calibration purposes. This has a repeat period of 64 s and allows 67 discrete wave components to be resolved from each dataset. In this procedure five input amplitudes were used (A = 4, 6, 8, 10 and 12 mm), 19 directions of propagation ($-45° < \theta < +45°$ in 5° intervals) and the surface elevation was again sampled at 12 positions. This gives a total of some 76 380 calibration points.

In the early stages of analysing these data, it became apparent that although the generation of very small wave amplitudes at the paddles has significant benefits, it also introduces unexpected difficulties. Evidence of this effect arose as a negative offset in the calibration curves, indicating that a small input voltage was required to overcome the inertia of the wave paddles. Indeed, in hindsight it is perhaps not surprising that, for very small excursions, a slightly larger force is required to accelerate a paddle from rest, when compared with the case of a paddle that is already moving. To overcome this small but very significant problem, the paddles were continuously excited by a high-frequency signal of low amplitude. Repeated tests confirmed that a 4 Hz signal, resulting in a wave of less than 1 mm in amplitude, was sufficient to remove the negative offset. Furthermore, detailed and repeated observations of the water-surface elevations confirmed that the waves arising due to this high-frequency signal were dissipated due to the effects of viscosity a significant distance upstream (*ca.* 2.5 m) of the measurement area.

(*c*) *Measurement procedure*

For each of the cases indicated in table 2, the linearly predicted focused time was set to 50 s after paddle start-up. All wave groups were focused on $y = 0$. For cases B and C (table 1*a*), the linearly predicted focal position was set at $x = 0$. In case D, the nonlinear shift in the focus position (see § 5) was large, so that the linear focus position was moved to $x = -0.7$ m. In all cases, the surface elevation was sampled simultaneously using 12 channels. Individual channels being sampled at 50 Hz for 49.94 s, commencing 30 s after paddle start-up. Given the repeatability of the wave conditions (see § 4 *d*), each wave group was sampled four times, with the gauges placed at different spatial positions. One wave gauge was kept at a pilot gauge position to verify the repeatability. Surface elevation data were thus measured at 45 spatial locations for each wave group. In each case, three wave gauges were placed at $(x, \pm y)$ for large values of y, in order to verify the symmetric properties of the wavefields. The remaining gauges were positioned such that the permutation of vector distances between the gauges was as widely distributed as possible. This latter arrangement ensures that the directional spectral resolution of the surface is as large as possible, within the limitations of the size of the measurement area and the total number of wave gauges (Goda 1985).

The velocity data recorded by the LDA were sampled at 1000 Hz for 6 s, commencing 47.0 s after paddle start-up. In each wave case, the wavefield was repeated a large number of times, with the LDA probe located at different vertical elevations beneath the position of the maximum wave crest. To guard against the possibility of large-scale recirculations becoming established within the wave basin, and decaying slowly with time, several measurements were made prior to the start-up of the wave paddles. The largest velocities recorded in these tests were less than 0.005 m s^{-1}. If this corresponds to a recirculation pattern, it is clear that it has no influence on the velocities recorded beneath the largest nonlinear wave groups.

(*d*) *Preliminary results*

The linear or near-linear wave groups indicated in table 2 ($A = 20$ mm) provide the best means of assessing the effectiveness of the calibration. Figure 3 concerns case D0420. Figure 3*a* provides a time-history of the water-surface elevation $\eta(t)$ recorded at the focal position, and contrasts the measured data with the linear prediction. Figure 3*b* provides a spatial description, measured along the x-axis, of the water-surface elevation at the instant of wave focusing $\eta(x)$. In contrast, figure 3*c* provides a spatial description perpendicular to the mean wave direction $\eta(y)$. In each of these figures, the measured data are in good agreement with the linear solution. Furthermore, in figure 3*b*, the pilot gauge located at $x = -0.7$ m indicates the variability in the repeated generation of one test case. This is clearly very small (± 0.5 mm) and consistent with the measurement errors discussed in § 3 *b* above. Figure 4 also concerns case D0420 and describes the vertical profile of the horizontal velocity (x com-

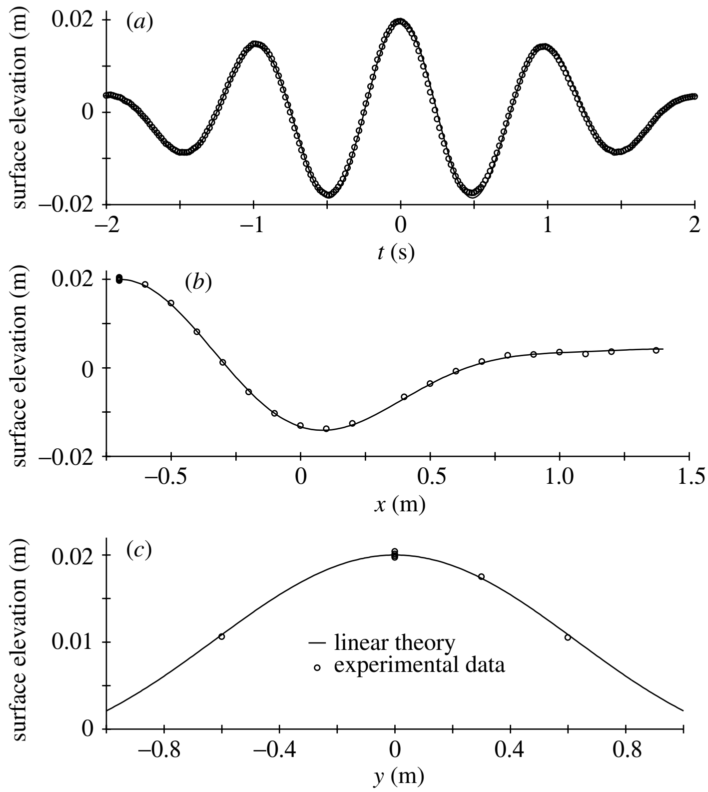

Figure 3. Comparisons with a linear ($A = 20$ mm) focused wave group, case D0420. (*a*) $\eta(t)$ at linear focal position. (*b*) $\eta(x)$ at linear focal time. (*c*) $\eta(y)$ at linear focal time.

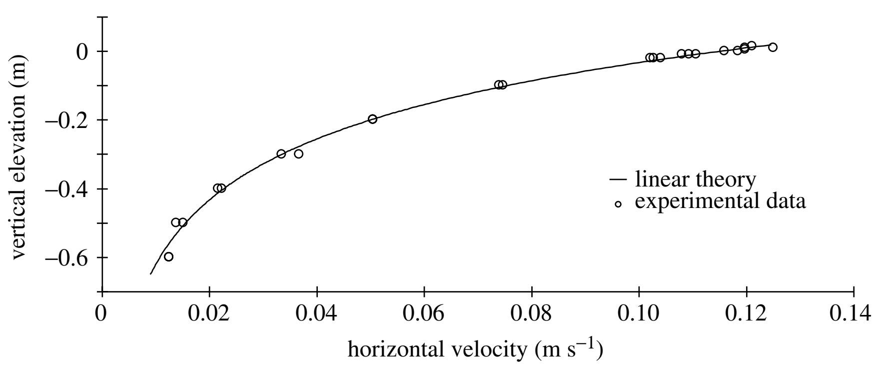

Figure 4. Horizontal velocity beneath a linear ($A = 20$ mm) focused wave group $u(z)$, case D0420.

ponent) recorded beneath the focused wave crest. Again, the agreement with linear theory is good. The data presented on figures 3 and 4 are representative of each of the linear wave groups described in table 2 and confirm the success of the calibration process. Further details concerning the experimental procedure and the preliminary results are given in Johannessen (1997).

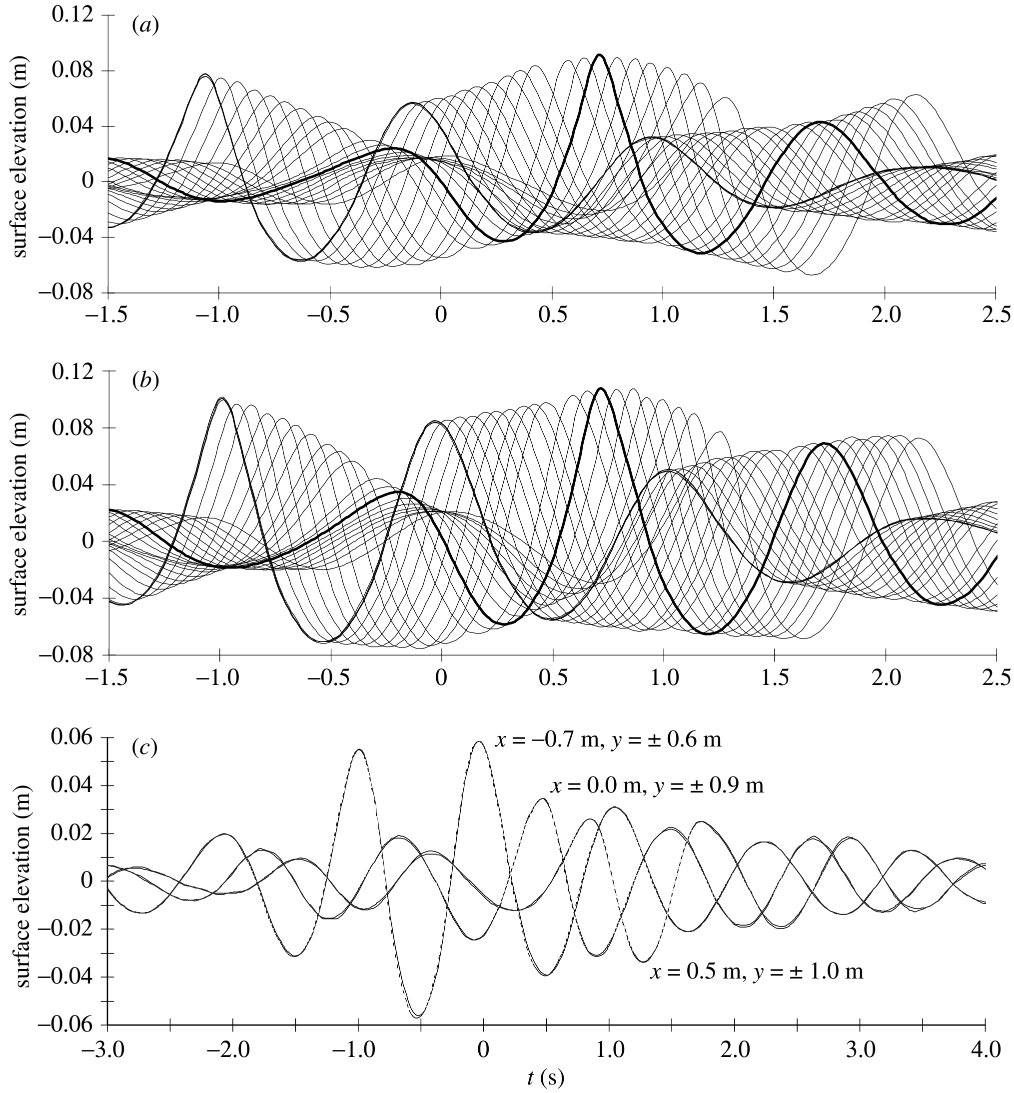

Figure 5. Temporal profiles of the water-surface elevation $\eta(t)$. (*a*) Centreline data ($y = 0$) for the unidirectional case Dud61. (*b*) Centreline data ($y = 0$) for the short-crested case D0493. (*c*) Symmetry of a wave group (case D0493).

5. Experimental results

(*a*) *Surface elevation*

The evolution of two highly nonlinear wave groups is considered in parts (*a*) and (*b*) of figure 5. Both cases concern the narrow-banded spectrum case D. The first (figure 5*a*) corresponds to a unidirectional group with an input amplitude of $A = 61$ mm (case Dud61), while the second (figure 5*b*) describes a short-crested group with $A = 93$ mm (case D0493). In each case, the waves are very close to the limit of wave breaking. Time-histories of the water-surface elevations recorded at 100 mm

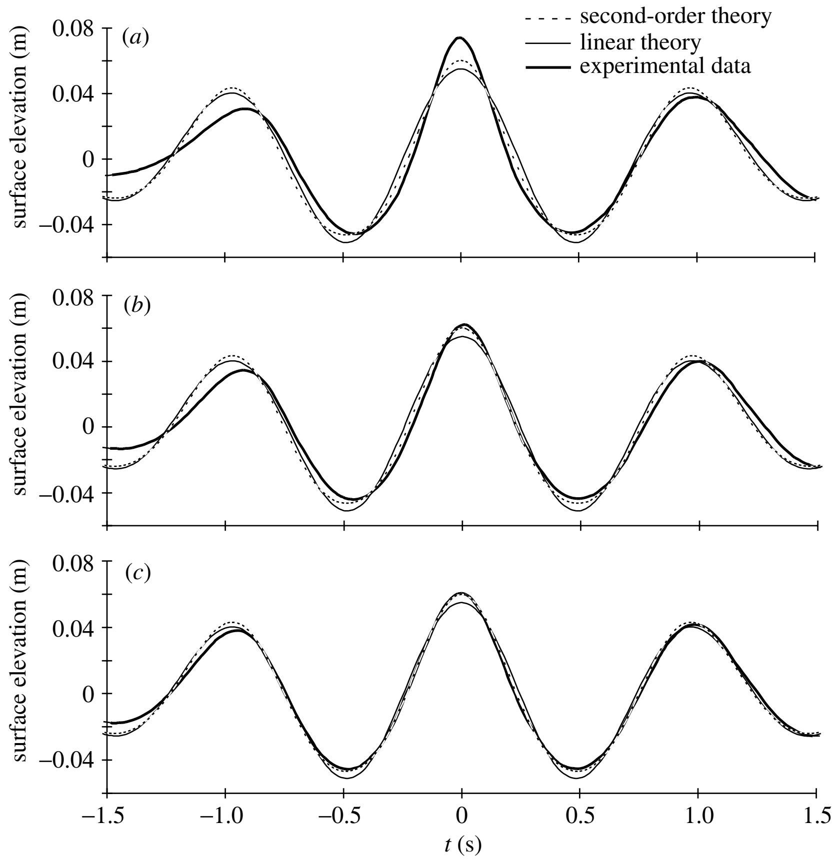

Figure 6. Profiles of the water-surface elevation at the position of the maximum crest elevation $A = 55$ mm. (*a*) Case Dud55. (*b*) Case D4555. (*c*) Case D0455.

intervals along the centre line of the measuring section ($y = 0$) confirm that a single global maximum crest elevation, indicated in bold, is identified. Furthermore, the wave gauges located closest to the wave paddles act as the pilot gauges discussed previously (cf. § 2). Multiple records, corresponding to repeated generations, are presented and the variations shown to be negligible. Indeed, it is satisfying to note that the RMS variation in the surface elevation recorded at the pilot gauge positions is not significantly larger than the RMS variation in the measurements of the still water level. Figure 5*c* again concerns case D0493 and contrasts wave gauge pairs located symmetrically about the x-axis. These data are representative of each of the test cases investigated. It confirms both the symmetry of the generated wavefields, and the absence of large unwanted spatial variations commonly associated with the generation of regular or irregular waves in a three-dimensional wave basin.

Parts (*a*)–(*c*) of figure 6 concern a unidirectional, a long-crested ($s = 45$) and a short-crested ($s = 4$) wave group, respectively, each with an input amplitude of $A = 55$ mm. Time-histories of the water-surface elevation $\eta(t)$ recorded at the position of the largest wave crest are compared with both a linear solution and a second-order solution based on the method of Sharma & Dean (1981). To facilitate these comparisons, the nonlinear shift in both the focus time and the focus position have been removed. Details of these nonlinear shifts in the focal position, both in space and time, are discussed in § 5 *c*. Comparisons between the parts of figure 6 confirm that the directionality of the wavefield has a significant influence on the nonlinearity of the largest wave event. For example, the highest crest observed in the unidirectional group (figure 6*a*) is 30% larger than the linear solution and 20% larger than the second-order predictions. In contrast, the maximum crest elevation observed in the short-crested group (figure 6*c*) is only 10% larger than the linear solution and most of this change (*ca.* 90%) is accounted for by the second-order solution.

Comparisons of this type are considered further on figure 9*a*. This concerns all of the test conditions given in table 2 and contrasts the maximum measured crest elevations, corresponding to an input amplitude of $A = 55$ mm, with the directional spread expressed in terms of $1/s$. With a constant input amplitude, it is clear that the largest nonlinear increase in the crest elevation arises in a unidirectional wave group ($1/s = 0$), and that this increase rapidly reduces as the directional spread increases. Indeed, the introduction of even a small directional spread ($s = 150$ or $1/s = 0.007$, corresponding to a very-long-crested sea state) appears to lead to a large reduction in the maximum crest elevation. It is shown in § 5 *e* that this effect represents a real weakening of the nonlinear wave–wave interactions due to the underlying directionality.

The observed reduction in nonlinearity with increasing directional spread is consistent with earlier theoretical calculations (Peregrine 1983). This study concerns the occurrence of wave jumps and caustics in finite-amplitude regular waves, based on solutions of the nonlinear Schrödinger equation. In relation to nonlinear focusing, it is briefly noted that many of the nonlinear properties, including the occurrence of an undular wave jump, depend upon the wave steepness, the degree of focusing and the scale of the focusing region, where the latter is clearly related to directionality. Further evidence of this is given by Stamnes *et al.* (1983) and was also observed in an experimental study of regular wave focusing briefly described by Peregrine *et al.* (1988).

Figure 7 again concerns the narrow-banded spectrum case D. Comparisons between the water-surface elevations $\eta(t)$ recorded at the position of the maximum crest elevation, and both linear and second-order theory are provided. In contrast to the data presented in figure 6, these wave cases correspond to the largest input-amplitude sums and are therefore very close to the limit at which incipient wave breaking occurs. Figure 7*a* concerns a unidirectional wave group, figure 7*b* a long-crested wave group and figure 7*c* a short-crested wave group. In each of these cases, it is clear that the central wave crest is higher and narrower than the linear solution, while the adjacent wave troughs are broader and less deep. However, in the unidirectional case (figure 7*a*), the second-order correction accounts for less than 25% of the difference between the linear solution and the measured data.

These results clearly suggest that the local increase in the maximum crest elevation cannot be accounted for by an essentially constant regime of free-wave components combined with their associated bound waves. Indeed, figure 7 highlights a significant change in the envelope of the wave group. This is evident from the lack of symmetry in the height of the wave crests either side of the maximum crest. This occurs in all three cases and appears to suggest that in a nonlinear wave group the largest wave crest moves towards the front of the group. As a result, the envelope of the wave group becomes asymmetric, and there is poor agreement between the mea-

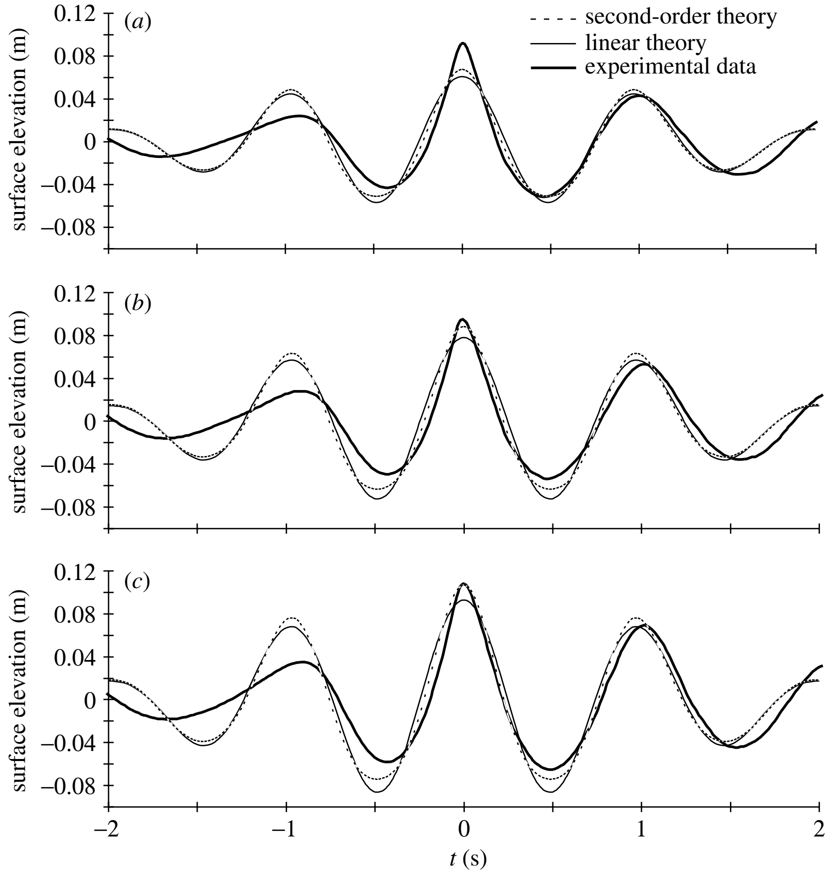

Figure 7. Profiles of the water-surface elevation at the position of the maximum (limiting) crest elevation. (*a*) Case Dud61. (*b*) Case D4578. (*c*) Case D0493.

sured and predicted waves recorded at the front of the group, $-2.0\,\mathrm{s} \leqslant t \leqslant -0.8\,\mathrm{s}$. Further evidence concerning nonlinear changes in the free-wave regime is given in § 5 *e*.

With increasing directional spread, two significant trends are identified. Firstly, a larger input amplitude is required to achieve a limiting condition. Secondly, although the absolute crest elevations are larger, their increase relative to first and second-order theory is much reduced. Indeed, in case D0493 the measured maximum crest elevation is in reasonable agreement with second-order theory, despite the fact that this wave is very close to its breaking limit. Qualitatively, these results appear consistent with the field observations reported by Jonathan & Taylor (1995). However, away from the central crest there are clear differences between the measured data and the model predictions. Indeed, careful observation also suggests that the central trough–trough period is reduced relative to the theoretical predictions. If it is assumed that the nonlinear interactions merely produce higher-order bound waves, this latter observation becomes difficult to explain.

Figure 8 provides spatial descriptions $\eta(x)$ of the largest wave crests observed in cases Dud, D45 and D04, with a range of input amplitudes. The times at which the

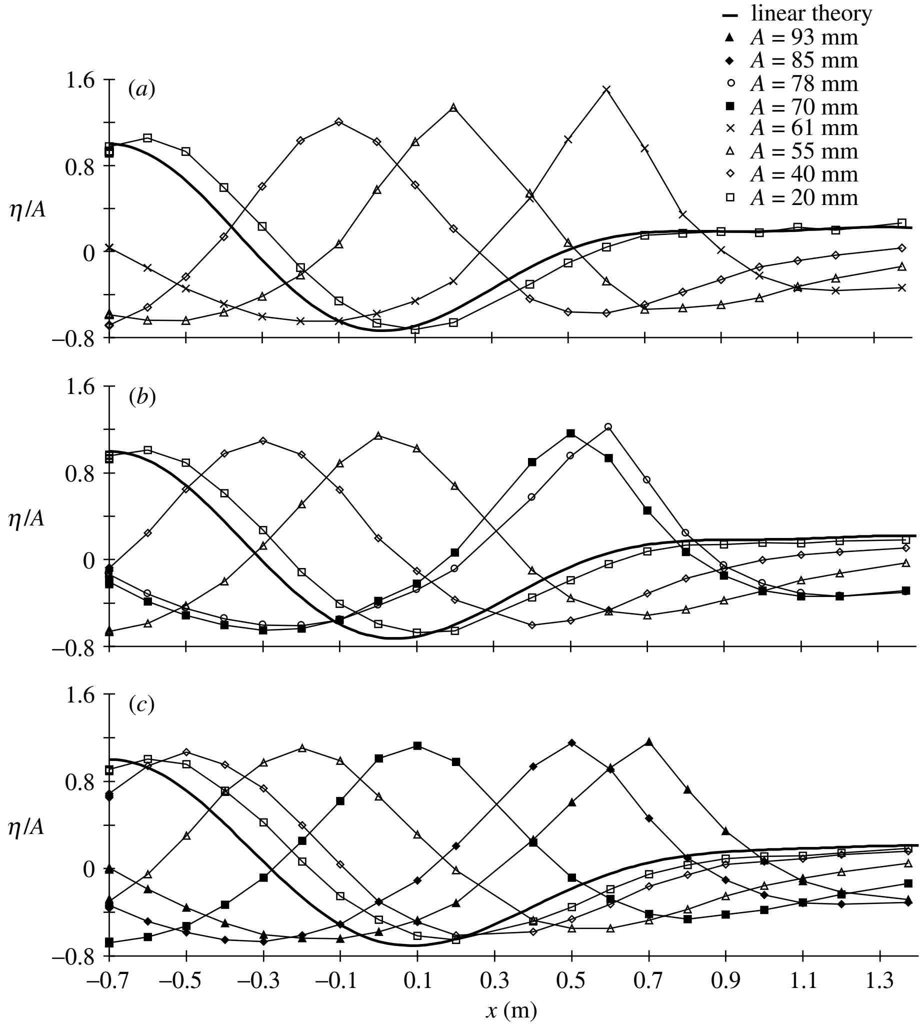

Figure 8. Normalized maximum surface elevations $\eta(x)$ for varying input amplitudes. (*a*) Case Dud. (*b*) Case D45. (*c*) Case D04.

data are presented is defined as the time at which the largest crest passes the wave gauge closest to the position of the maximum crest elevation. To aid comparisons, the surface elevation is non-dimensionalized with respect to the linear sum of the component amplitudes A. Although the resolution of the surface elevation in the spatial domain is reduced relative to the description in the time domain, the down-stream shifting of the maximum crest is clearly established, as is its dependence on the input amplitude. Furthermore, in figure 8*a*, the nonlinear increase in the crest elevation is well defined, while in parts (*b*) and (*c*) of figure 8, its reduction with increasing directionality is clearly apparent.

The near-limiting wave cases considered on figures 7 and 8, together with the equivalent cases arising in the other frequency spectra (B and C), are reconsidered in parts (*b*) and (*c*) of figure 9. In figure 9*b*, the maximum limiting crest elevation is

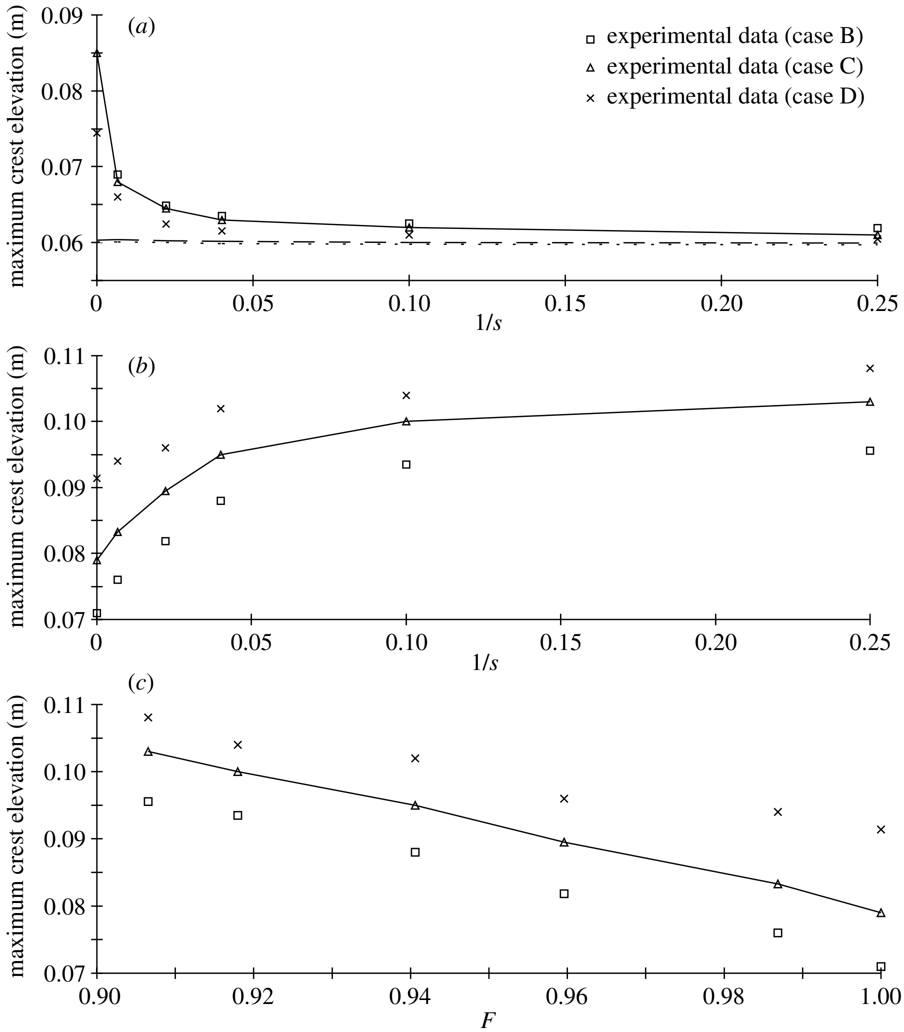

Figure 9. Global maximum crest elevations. (a) Constant input amplitude $A = 55$ mm. (b) At the breaking limit $\eta_{\max}$ versus $1/s$. (c) At the breaking limit $\eta_{\max}$ versus F.

expressed as a function of the directional spread, represented by $1/s$. Whereas figure 9a suggests that, for a given linear-amplitude sum ($A = 55$ mm), the maximum crest elevation reduces with increasing directional spread, figure 9b suggests that increasing directionality allows larger limiting crest elevations. If one assumes that both the local nonlinear increase in the crest elevation and the limiting condition at which wave breaking first occurs is dependent upon some measure of the local wave steepness, the importance of directionality becomes clear. In a unidirectional sea, the wave steepness is constrained within a single plane (aligned with the direction of wave propagation) and consequently yields the maximum local steepness for a given linear-amplitude sum A. In contrast, in a directionally spread wavefield, with individual wave components focused at a single point, the steepness associated with these components is located on a large number of intersecting planes. As a result, an increase in the directionality leads to a reduction in the in-line wavefront steepness. This, in turn, allows larger linear-amplitude sums prior to the onset of wave breaking.

As an alternative to figure 9*b*, the directional bandwidth may be characterized by the in-line velocity reduction factor F, rather than $1/s$. F is defined by

$$F = \sum_{m=1}^{M} b_m \cos(\theta_m). \tag{5.1}$$

In a linear sense, this parameter also provides guidance as to the reduction in the in-line (x component) wave steepness due to the underlying directionality. In figure 9*c* it is clear that as F reduces, indicating a larger directional spread, the maximum limiting crest elevation increases. Indeed, in the most short-crested events ($F = 0.907$ or $s = 4$), the maximum crest elevation may be in excess of 30% larger than the equivalent values in a unidirectional event. Furthermore, comparisons between the data presented in figure 9*c* suggest that the effect of directionality on the maximum limiting crest elevation appears to be relatively insensitive to the underlying frequency distribution ($\partial\eta_{\max}/\partial F \approx$ const.).

These results are in broad agreement with earlier theoretical calculations, in which Roberts (1983) considered the interaction of two regular wave trains of equal wavelength and equal amplitude propagating at an angle to each other. Their combination produces a short-crested wave pattern that is periodic in both the direction of wave propagation and the perpendicular horizontal direction. After applying a perturbation expansion and summing the terms to high order, Roberts showed that highly nonlinear short-crested waves may be up to 60% steeper than two-dimensional progressive waves.

Although such waves are clearly very different from the transient focused waves considered in the present study, our results suggest that in the most short-crested events ($s = 4$), the wave steepness represented by $\eta_{\max}k_{\mathrm{p}}$ (where k_{p} is the wavenumber corresponding to the peak of the spectrum) is *ca.* 35% larger than the corresponding value for unidirectional waves.

(*b*) *Water-particle kinematics*

A typical example of the velocity data gathered beneath one wave group (case D0493) is presented in figure 10. No manipulation of these data has been undertaken and each data trace $u(t)$ results from one generation of the wave group. The continuous data traces are recorded beneath the level of the lowest wave trough, $z \leqslant -0.07$ m, while the intermittent traces are recorded above. At two elevations ($z = 0.0, 0.06$ m), multiple traces are presented to confirm the repeatability of the measuring procedure. In this case, the maximum crest elevation was $\eta_{\max} = 0.108$ m, and reliable data were recorded within 8 mm of this maximum (i.e. $z = 0.1$ m).

Figure 11 provides three examples in which the vertical profile of the maximum horizontal velocity, arising beneath the largest wave crest, is compared with both a linear and a second-order solution. The three cases are, respectively, Dud61, D4578 and D0493. These correspond to the limiting conditions investigated in figure 7 and involve increasing directional spreads. In the unidirectional case (figure 11*a*), the near-surface velocities are significantly larger than either of the theoretical solutions.

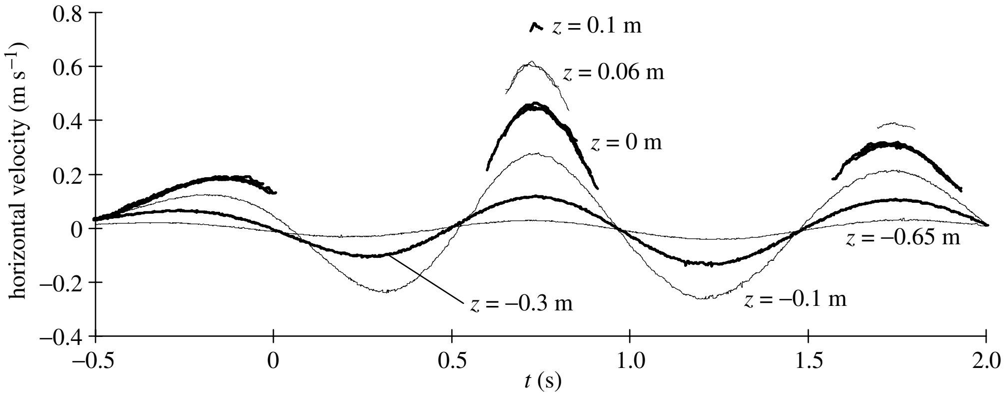

Figure 10. Temporal traces of horizontal velocity $u(t)$, case D0493.

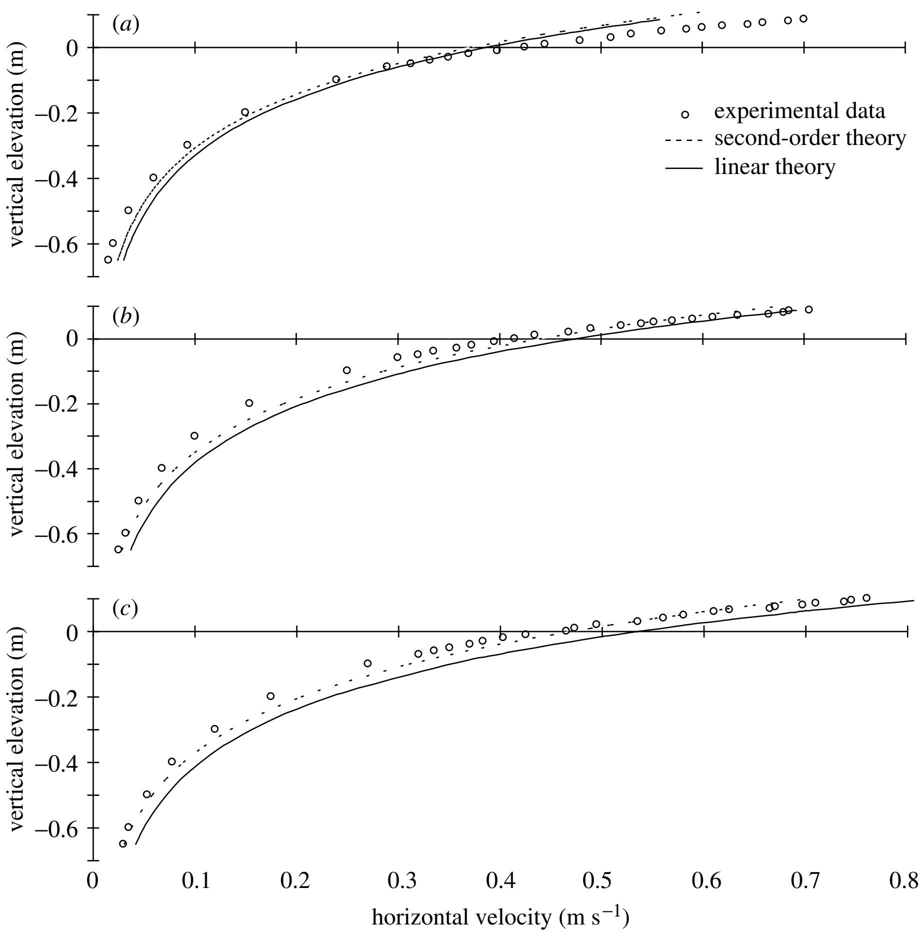

Figure 11. Horizontal velocity profiles $u(z)$ beneath three limiting wave cases. (a) Case Dud61. (b) Case D4578. (c) Case D0493.

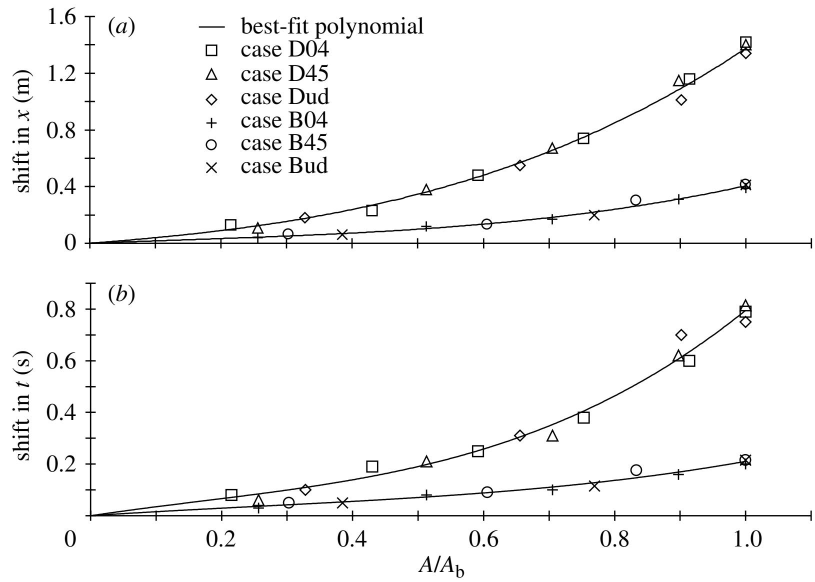

Figure 12. Shift in position of the maximum crest elevation. (a) Shift in space along centreline. (b) Shift in time.

This is consistent with the increased crest elevations identified on figure 7a and is further discussed by BST. More importantly, the present results confirm that relative to the theoretical solutions the extreme near-surface velocities reduce with increasing directionality. Indeed, with a large directional spread ($s = 4$ in figure 11c), the near-surface velocity data lie between the linear and the second-order solution. However, at greater depths beneath the water surface, where one would perhaps expect better agreement with the second-order solution, there is evidence of a reduction in the fluid velocity. This effect appears to increase with the directionality of the wavefield. Furthermore, it is also interesting to note that despite the differing characteristics of these three limiting wave cases, the vertical profiles of the in-line velocities are surprisingly similar.

(c) *Focal characteristics: position, phase velocity and dispersion*

When a nonlinear focused wave group evolves in a two-dimensional wave flume, BST showed that there is a downstream shifting of the focus position, relative to linear theory, with a corresponding increase in the focus time. Earlier studies of breaking waves (Longuet-Higgins 1974; Rapp & Melville 1990; Skyner 1996), again conducted in two-dimensional wave flumes, identified a similar effect. In the present study, a nonlinear shift in both the focal position and the focal time was observed for each of the test cases (see, for example, figure 8). However, if one assumes that the nonlinearity of the wave event may be approximated by the ratio A/A_{b}, where A is the linear sum of the component wave amplitudes and A_{b} is its limiting value just prior to the onset of wave breaking (see table 2), the nonlinear shifts in the focal event appear to be strongly dependent upon the underlying frequency spectrum, but independent of the directional spread. Figure 12a concerns both the narrow and the broad-banded frequency spectra (cases B and D) and contrasts the spatial shift in

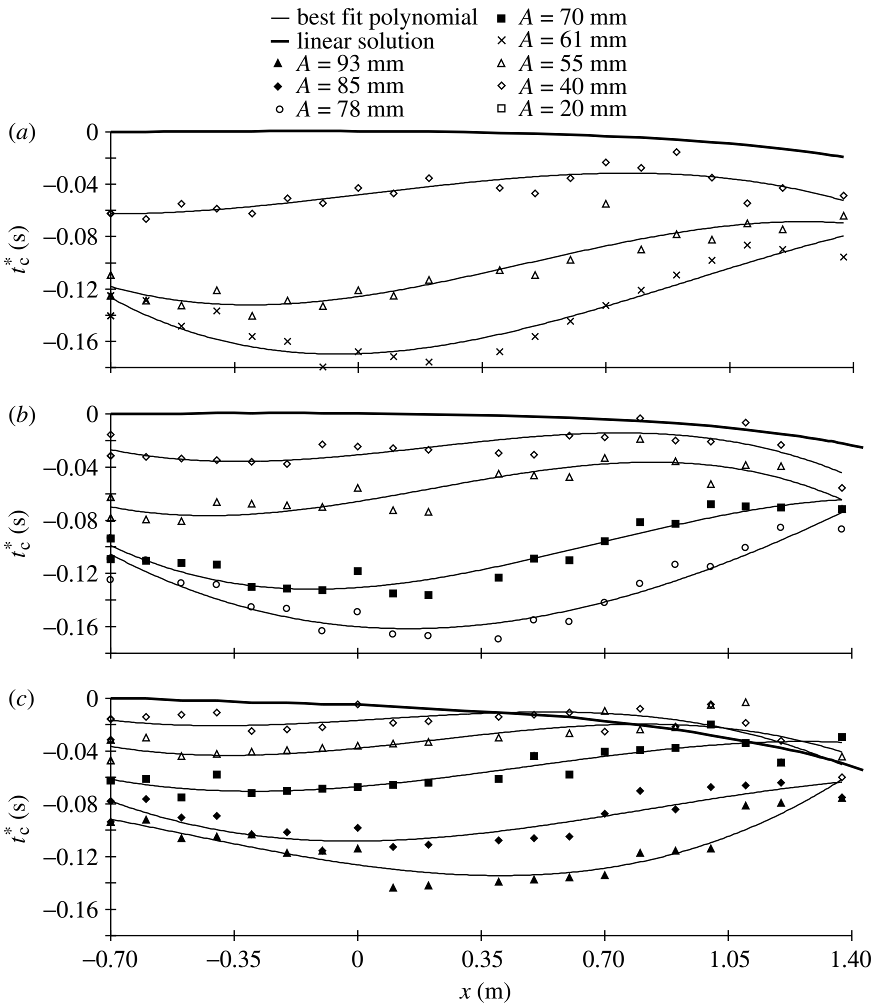

Figure 13. Temporal position of extreme crest along centreline t_c^* versus x on $y = 0$.

the focal position for three directional spreads ($s = \infty$, $s = 45$ and $s = 4$) and a wide range of input amplitudes. Figure 12*b* provides similar comparisons describing the shift in the focal times.

These results suggest that the nonlinear mechanisms that govern the evolution of a focused wave group are independent of the directional spread if wave groups equally close to their breaking limit are considered. Furthermore, BST suggest that the shift in the position of the maximum crest may be attributed simply to the nonlinear increase in the crest velocity arising due to its increased size. If this were indeed the case, one would expect the shift of the focal event to be strongly dependent on directionality, since a large wave event arising in a unidirectional sea exists for longer times when compared with the rapid dispersion associated with a short-crested wave group.

Within the present tests, the resolution of the wavefield along the centre line of the measurement area offers the opportunity to investigate the changes in the crest

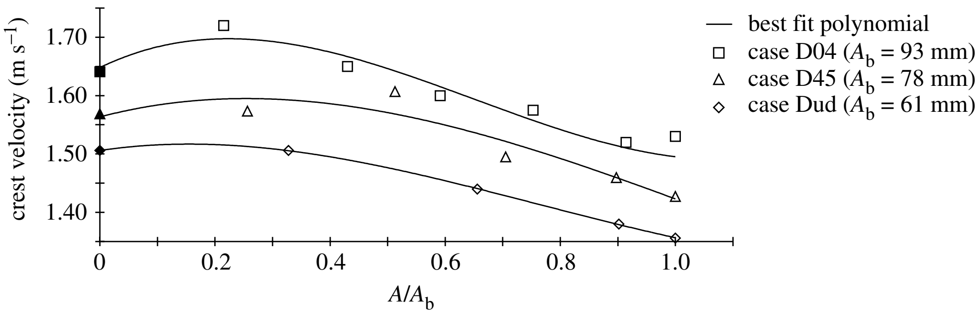

Figure 14. Crest velocity at the position of the maximum crest elevation.

velocity as the extreme wave crest evolves. Figure 13 concerns the three narrow-banded wave cases (Dud, D45 and D04) considered in figure 8. The linear focal position is set to $x_\mathrm{f} = -0.7$ m for these cases. If t_c denotes the time at which the extreme crest passes an individual wave gauge located on the centre line, t_c^* is defined by subtracting a simple linear function,

$$t_\mathrm{c}^* = t_\mathrm{c} - \frac{(x + 0.7)}{u_\mathrm{l}}, \tag{5.2}$$

where u_l is the linearly predicted crest velocity at $x = -0.7$ m. For visual clarity, t_c^*, rather than t_c, is plotted against x in figure 13.

The data presented in figure 13 clearly show that at the smallest values of x (i.e. upstream of the focal position), the largest crest arises before the linearly predicted values ($t_\mathrm{c}^* < 0$). This is consistent with the expected nonlinear increase in the crest velocity. However, the positive gradients of t_c^* (i.e. $\partial t_\mathrm{c}^*/\partial x > 0$) observed in figure 13 in the vicinity of the extreme events imply a reduction in the crest velocity relative to its linearly predicted value at the linear focal position u_l. Although there is inevitably some scatter in these data, the reduction in the crest velocity is clearly identified. Indeed, the effect is observed for all wave groups, becoming more significant as the nonlinearity of the group increases. For the steepest wave groups there is an initial tendency for the crest to move faster than the linear prediction. However, as the position of the maximum crest elevation is approached, the gradient of t_c^* changes sign and the crest velocity reduces.

Using the data presented in figure 13, the crest velocity at the position of the maximum crest elevation may be computed. The results, expressed as a function of A/A_b, are given in figure 14, where the closed symbols at $A/A_\mathrm{b} = 0$ are based on linear calculations (u_l). The parameterA/A_b, where A_b is the largest input value specified in table 2, was adopted since many of the envelope properties of the wave group appear to be independent of the directional spread, provided wave groups equally close to the breaking limit are considered (see also figures 12 and 19). A/A_b provides an effective measure of the proximity to the breaking limit. In contrast, a simple measure of the wave steepness, $\sum a_n k_n$, was found to be dependent upon the directional spread. In the most nonlinear cases the reduction in the crest velocities are significant, ranging from 10% of u_l in the unidirectional case to 7% of u_l for the most directionally spread case. The data presented in figure 14 suggest that while a small increase in the crest velocity, relative to linear theory, arises at relatively low

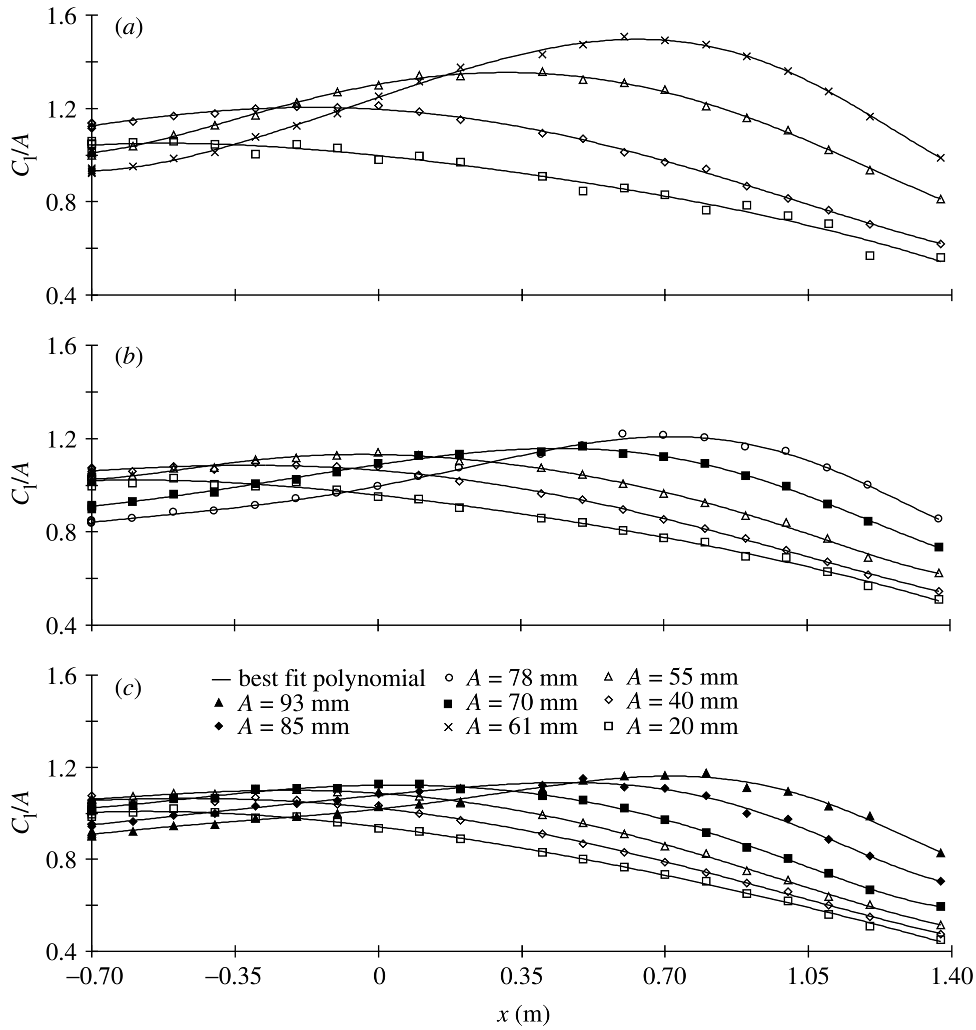

Figure 15. Evolution of extreme crests along the centreline $y = 0$. (a) Case Dud. (b) Case D45. (c) Case D04. (Note: C_l denotes the local crest elevation.)

wave steepness, an overall reduction in the crest velocity becomes dominant in the vicinity of the global maximum if the wave group is strongly nonlinear.

In seeking an explanation for these results, it is necessary to consider the possibility of significant changes in the free-wave regime. Within the present discussion, free-wave components are defined as wave components that satisfy, or nearly satisfy, the linear dispersion relationship (equation (4.2)). For example, an increase in the central frequency of the free-wave regime, due to a rapid broadening of the free-wave spectrum in a highly nonlinear wave group, would be consistent with the present results. Furthermore, the observed reduction in the central trough-to-trough period of the water-surface elevation (figure 7) is also consistent with this view. Similarly, such a change would also explain the observed reduction in the horizontal velocity at intermediate depths (figure 11).

In both linear and nonlinear wavefields, a unidirectional wave group will assemble and disperse more slowly than an equivalent group with the same frequency–amplitude spectrum but significant directional spread. In a linear formulation, the rate of dispersion will be symmetric about the focused event. Figure 15 again concerns the narrow-banded frequency spectrum (Dud, D45 and D04) and provides data recorded along the x-axis for a variety of input amplitudes. In each case, the data define the maximum local crest elevation η_{max}, irrespective of the time at which it occurs. These results clearly indicate that the evolution of a wave group is asymmetric either side of the global maximum. This result is particularly evident in the most nonlinear cases, involving the largest input amplitudes, and suggests an asymmetric wave group envelope such that the rate of dispersion is more rapid after the global maximum than it was before it. This effect cannot be explained by the development of large bound wave components, since these simply propagate at the speed of the associated free waves and do not therefore affect the dispersive properties of the wave group. Alternatively, a rapid widening of the free-wave regime in the vicinity of the global maximum would explain the observed increase in the rate of dispersion.

Significant energy redistributions and, in particular, changes in an initial free-wave regime due to the focusing of wave components have been reported by other researchers. For example, Whalin (1972) considered the focusing, or convergence, of a unidirectional regular wave train due to local changes in the bottom topography involving parallel circular contours. Although these results are complicated by the simultaneous occurrence of wave refraction and diffraction, the nonlinear transfer of wave energy from the lower- to the higher-frequency components is clearly identified. Furthermore, Whalin (1972) also provides additional phase information that suggests at least some of the nonlinear harmonics are uncoupled from the fundamental frequency and therefore correspond to changes in the free-wave regime.

(*d*) *Comparisons with inverted wave groups*

To further investigate the occurrence of freely propagating wave components, a number of focused wave groups have been compared with their corresponding inverse groups. In the latter cases, the amplitude of the component waves, a_n in (4.1), are all negative and the group corresponds to the linear focusing of wave troughs rather than wave crests. This approach was previously adopted by BST and provided valuable insight into the nonlinear properties of focused wave groups. Figure 16 concerns the narrow-banded spectrum with a large directional spread (case D04), and provides comparisons between the water-surface elevations recorded at the linear focal position. Six amplitude sums are considered, ranging from $A = 20$ mm to the limit of incipient wave breaking at $A = 93$ mm. In each case, the data are non-dimensionalized with respect to the input amplitude A, and the record corresponding to the inverse wave group $\eta^*(t)$ is presented as $-\eta^*(t)$, so that the large wave trough occurring in the vicinity of $t = 0$ appears as a wave crest. Comparisons are also made with linear theory. For small amplitude sums, the focused wave group $\eta(t)$ and the inverse focused wave group $-\eta^*(t)$ are effectively identical and in good agreement with the linear solution. However, as A increases, the measured data show significant departures, with the crests of the focused wave groups becoming higher and narrower and the troughs of the inverse groups becoming wider than the linear prediction. Such changes are to be expected and may be attributed to the nonlinear components bound to the freely propagating waves.

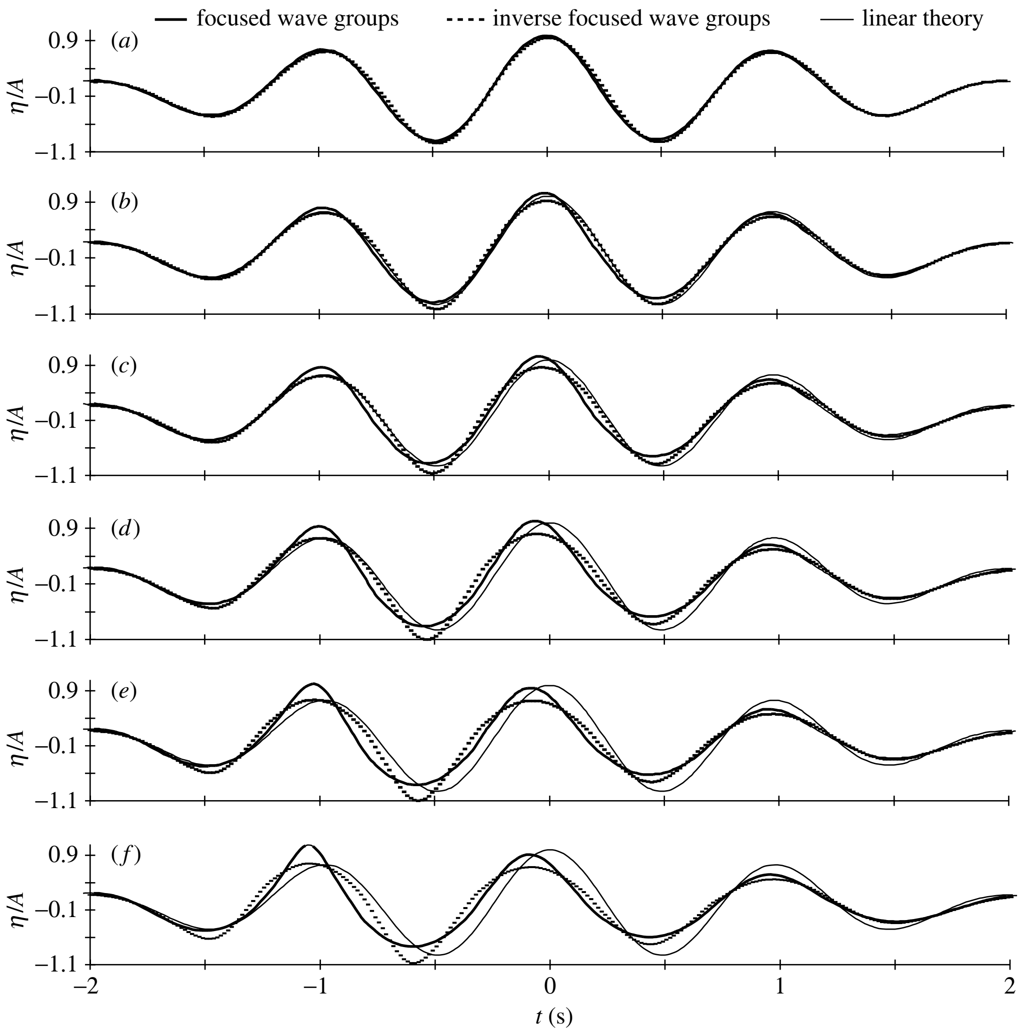

Figure 16. Focused and 'inverse' focused wave groups at the linear focal position, case D04. (*a*) $A = 20$ mm. (*b*) $A = 40$ mm. (*c*) $A = 55$ mm. (*d*) $A = 70$ mm. (*e*) $A = 85$ mm. (*f*) $A = 93$ mm.

While the crest–trough asymmetry is clearly significant, comparisons between the measured data and the linear theory highlight a separate effect. It has already been noted that a possible explanation for a shift in the focal position, in both space and time, is a modification of the free-wave regime. If this is indeed the case, figure 16 suggests that such changes are independent of the sign of A, since both the focused and the inverse focused wave groups occur at the same position in time. Indeed, if one neglects the crest–trough asymmetry associated with the bound waves, the deviations from linear theory are remarkably similar. This implies that large deviations from linear and second-order theory are predominantly related to the nonlinear evolution of the wave group envelope involving rapid changes in the free-wave regime.

In general terms, the notion of a free-wave regime may be introduced,

$$\eta_{\mathrm{f}} = \sum_{n=1}^{\infty} a_n(t)\cos(k_n x - \omega_n t + \varepsilon_n(t)), \tag{5.3}$$

where the component wave amplitudes a_n and the phase shifts ε_n may vary with time. The nonlinear surface profile is defined as

$$\eta = \eta_{\mathrm{f}} + \eta_{\mathrm{b}}, \tag{5.4}$$

where the bound wave regime η_{b} is to be expressed as

$$\eta_{\mathrm{b}} = \sum_{n=1}^{\infty}\sum_{m=1}^{\infty} a_n a_m F_{nm}^{2} + \sum_{n=1}^{\infty}\sum_{m=1}^{\infty}\sum_{l=1}^{\infty} a_n a_m a_l F_{nml}^{(3)} + \cdots . \tag{5.5}$$

It is assumed that the bound waves are completely specified in terms of the free waves and that the F coefficients are independent of a. It is further assumed that η_{b} modifies the wave profile given by η_{f} without shifting the position of a crest or a trough in space or time. Within this description, the first term on the right-hand side of (5.5) represents the second-order two-wave wavenumber sum and wavenumber difference interactions (Longuet-Higgins & Stewart 1960; Sharma & Dean 1981), whereas the second term represents the third-order non-resonant three-wave interactions.

In the present paper we merely wish to argue that if, as figure 16 suggests, η_{f} remains equal in magnitude but opposite in sign for a focused and an inverse focused wave group, the following relations apply:

$$\tfrac{1}{2}(\eta - \eta^{*}) = \eta_{\mathrm{f}} + \sum_{l=1}^{\infty}\sum_{n=1}^{\infty}\sum_{m=1}^{\infty} a_n a_m a_l F_{nml}^{(3)} + \cdots \quad \text{(odd terms)}, \tag{5.6 a}$$

$$\tfrac{1}{2}(\eta + \eta^{*}) = \sum_{n=1}^{\infty}\sum_{m=1}^{\infty} a_n a_m F_{nm}^{(2)} + \cdots \quad \text{(even terms)}. \tag{5.6 b}$$

In figure 17 these relations are used to isolate terms involving even and odd powers of a. Parts (a) and (b) of figure 17 concern cases Dud61 and D0493, respectively, and contrast the results of (5.6 a) with the linearly predicted solution based on the input spectrum. The difference between the linear solution and $\frac{1}{2}(\eta-\eta^{*})$ is clearly too large to be associated with third-order non-resonant interaction terms, thereby implying that, in the vicinity of the large wave event, there is a change in the free-wave regime. In contrast, parts (c) and (d) of figure 17 compare the results of (5.6 b) with the second-order solution based on the input spectrum. Cases Dud61 and D0493 are again considered and the difference between the second-order solution and $\frac{1}{2}(\eta+\eta^{*})$ shown to be too large to be accounted for in terms of fourth-order effects, but consistent with a second-order correction to a modified regime of free waves. The results presented in figure 17 are representative of each of the frequency spectra (B, C and D) and may indicate that there are significant changes in wave components that satisfy, or nearly satisfy, the linear dispersion relationship in the vicinity of a large highly nonlinear wave event.

Further evidence of this effect is provided by the depth of the focused wave trough (η^{*}_{min}). In each of the unidirectional wave cases, the data presented in table 3 suggest that the focused wave trough is deeper than the linear-amplitude sum ($\eta^{*}_{\mathrm{min}} < -A$).

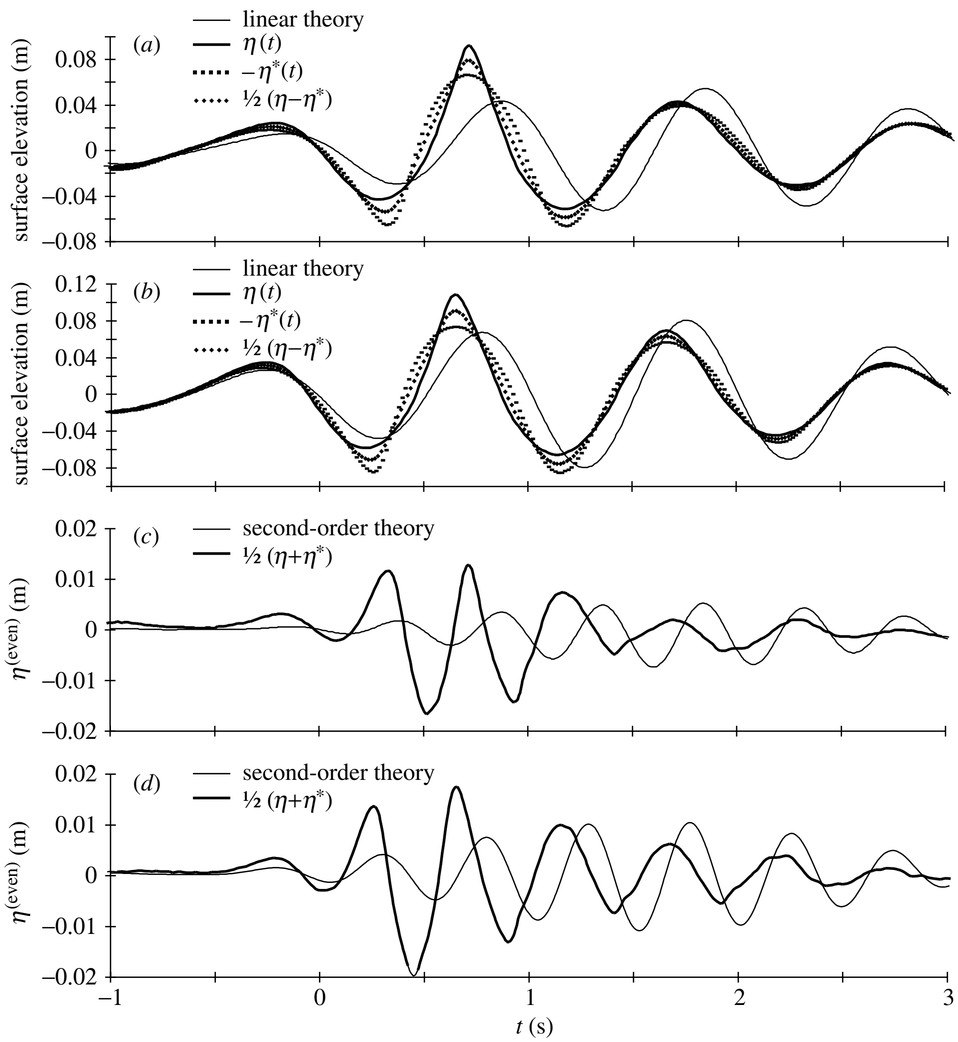

Figure 17. Focused and 'inverse' focused wave groups at the position of the maximum crest. (*a*) Case Dud61. (*b*) Case D0493. (*c*) Case Dud61. (*d*) Case D0493.

Table 3. *Surface elevations recorded in focused, $\eta(t)$, and 'inverse' focused, $\eta^*(t)$, wave groups*

wave spectrum	directional spectrum	input amplitude A (mm)	$\eta_{\max}$ (mm)	$-\eta^*_{\min}$s (mm)
B	$s = \infty$ (unidirectional)	52	71	56
B	$s = 4$ (short-crested)	78	96	69
D	$s = \infty$ (unidirectional)	61	92	67
D	$s = 4$ (short-crested)	93	108	73

While the presence of significant bound waves may lead to increases in the maximum crest elevation, they should lead to a reduction in the depth of the wave trough. However, if it is accepted that changes in the free-wave regime are possible, the data given in table 3 may be explained.

At this point, it is important to note that many of the effects identified in this and earlier sections, §§ 5 *a*–*d*, may be explained, at least qualitatively, by the application of modulation theory based on the nonlinear Schrödinger equation for deep water waves and its extension proposed by Dysthe (1979). For example, Taylor & Haagsma (1994) considered the narrow-banded unidirectional wave group reported by BST (case Dud55 using present notation) and showed that the nonlinear evolution equations indicate qualitatively similar asymmetry in the shape of the wave envelope and the shifts in the position of the maximum crest elevation. More recently, Henderson *et al.* (1999) have considered long time-evolution of unidirectional periodic deep water waves subject to small amplitude modulation. Full numerical calculations, based on Dold & Peregrine (1984), are successfully compared with the Dysthe equation. Indeed, they conclude that these results give encouragement for the use of the nonlinear Schrödinger equation in three-dimensional wave modelling.

(*e*) *Frequency spectra and energy redistribution*

The distribution of wave components in the frequency domain may be deduced by applying a standard Fourier transform to the time-histories of the water-surface elevations recorded at the position of the maximum crest elevation. If the data recorded contain only one extreme event, as is the case in the present study, a Fourier transform will accurately resolve the frequency components that contribute to the formation of this event. Figures 18 and 19 provide output from such an analysis. Figure 18 concerns the narrow-banded spectrum (case D), with an input amplitude of $A = 55$ mm and four directional spreads ranging from unidirectional to very short-crested ($s = 4$). In each case, the amplitude spectrum derived from the measured data are compared with the input spectrum outlined in § 4. The frequency range corresponding to the second-order frequency-sum terms (Longuet-Higgins & Stewart 1960) based on the input spectrum is also indicated. In light of the previous discussion, these results are highly informative. In the unidirectional case (figure 18*a*), there is a clear redistribution of energy from within the input range to frequencies that lie immediately above its upper limit. In the narrow-banded spectrum (case D), this energy is clearly identified since it lies between the distinct regions defining the input spectrum and the second-order frequency-sum terms. Whereas existing theories cannot account for this energy, the present study suggests that this represents a broadening of the free-wave regime. If this is so, and it cannot be conclusively proven on the basis of this experimental study, it explains the very large increase in the crest elevations observed in figure 6*a*. Furthermore, if one considers figure 18, involving progressively larger directional spreads, it is clear that the extent of this energy redistribution reduces rapidly. This reduction may be due to the reduced wavefront steepness arising in a directionally spread sea. As the energy redistribution reduces, so does the potential for significantly increased crest elevations. This is consistent with the data shown in figure 9*a*. For example, in the most short-crested test case ($s = 4$ in figure 18*d*), the fact that there is almost no widening of the free-wave regime suggests that a second-order solution, based upon the input conditions, should provide a good description of

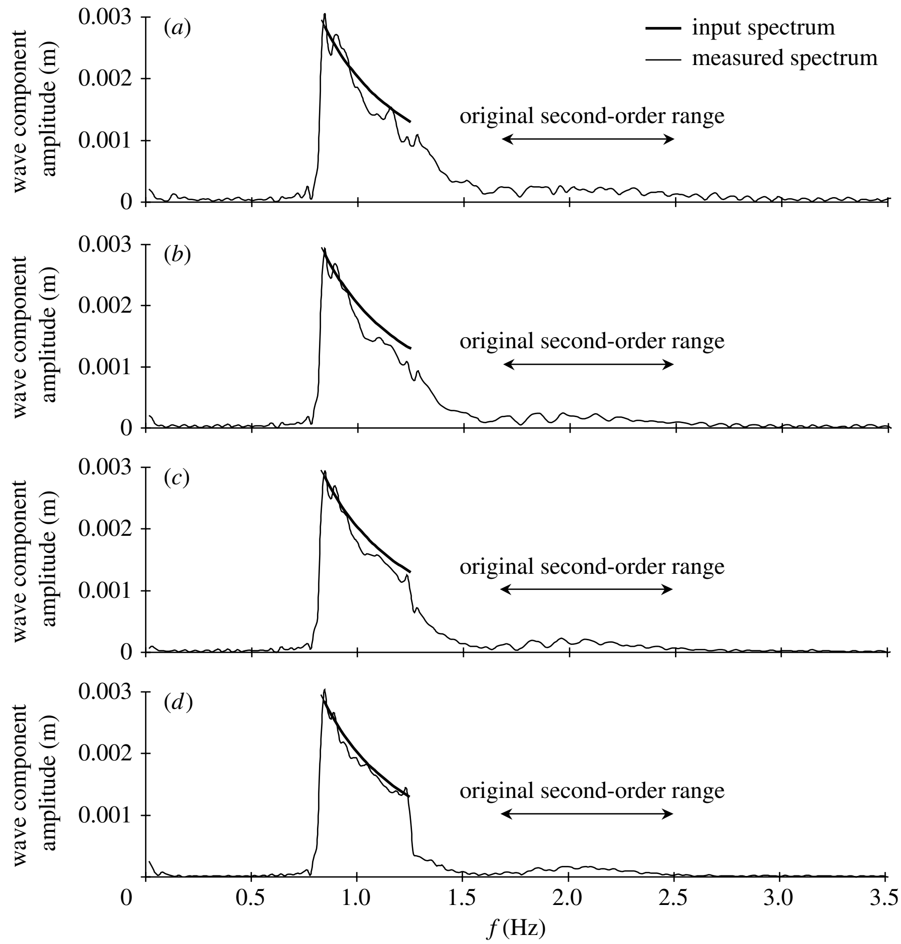

Figure 18. Frequency–amplitude spectra derived at the position of the maximum crest elevation with a constant input amplitude $A = 55$ mm. (*a*) Case Dud55. (*b*) Case D15055. (*c*) Case D4555. (*d*) Case D0455. (Note: fundamental period 64 s.)

both the water-surface elevation $\eta(t)$ and the associated water-particle kinematics. Figures 7*c* and 11*c* confirm that this is indeed the case.

Figure 19 provides similar amplitude spectra for the limiting wave cases observed in each of the three frequency spectra (B, C and D). In each of these figure parts, several amplitude spectra, corresponding to the various directional spreads, are overlaid. These results suggest that for each frequency–amplitude spectrum (B, C and D), the amplitudes of the wave components outside the initial input range are independent of the directional spread. Furthermore, the differences that cause or allow the larger crest elevations to evolve in a directional wavefield (parts (*b*) and (*c*) of figure 9) are clearly apparent within the input range (i.e. the larger the directional spread, the larger the energy within the input range, and hence the higher the maximum wave crest).

One possible interpretation of these results suggests that the limiting wave conditions, occurring just prior to the onset of wave breaking, are largely dependent

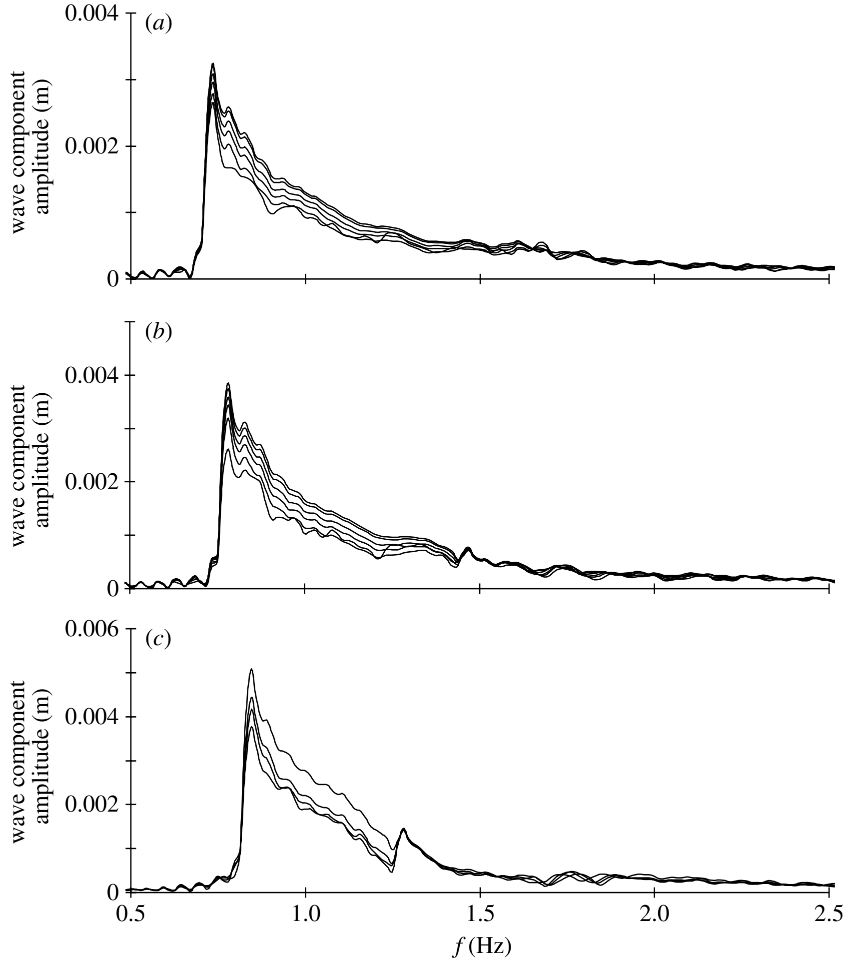

Figure 19. Frequency–amplitude spectra based on the limiting wave conditions with varying directional spreads. (*a*) Case B. (*b*) Case C. (*c*) Case D. (Note: directional spreads correspond to $s = \infty$ or unidirectional $s = 150$, 45, 25, 10 and 4.)

upon the generation of sufficient nonlinear wave components (involving both free and bound waves) arising outside the initial input range. Once this threshold is reached, the wave breaks. This condition may perhaps also be defined in terms of some limiting in-line crest-front steepness. In the case of a directional wavefield, the overall reduction in nonlinearity, or crest-front steepness, requires more energy within the input range to achieve this necessary threshold. Accordingly, the limiting waves are larger than those arising in a unidirectional sea.

The results presented in figure 19 may also be related to the equilibrium range of a wave spectrum (Phillips 1977, 1985). It has long been known that, provided they are properly scaled, the high-frequency and high-wavenumber parts of a wave spectrum collapse on to universal curves. When considering field data, the equilibrium range begins at approximately three times the peak of the spectrum, where the wave components are dominated by the nonlinear interactions. In the present cases, a similar pattern emerges immediately outside the initial input range. The self-similarity within this range is believed to be due to the existence of sharp crests in breaking or near-breaking waves. This singular or near-singular geometry has a controlling influence on the shape of the tail of the spectrum. Recent investigations of this phenomenon include Belcher & Vassilicos (1997). In the present experiments, it is interesting to note that the controlling influence of the near-singular geometry appears to be independent of the directional spread.

6. Concluding remarks and practical implications

A new experimental study has been described in which large isolated wave groups were generated in a laboratory wave basin. These events were produced by the focusing of wave components at one point in space and time, and involve a spread of wave energy in both the frequency and the directional domains. A focusing event of this type is believed to be of considerable practical importance, since it provides a realistic mechanism for the development of an extreme wave appropriate to the design of both offshore structures and vessels. By varying the component wave amplitudes, wave groups ranging from near-linear to the limit of incipient wave breaking were recorded. The primary purpose of these tests was to clarify the influence of directionality on the nonlinear characteristics of these extreme wave groups. To achieve this, measurements of the water-surface elevations and the underlying water-particle kinematics were recorded.

The measured data confirm that the directionality of a wavefield has a profound effect upon the nonlinear dynamics of a focused wave group. This, in turn, provides a plausible explanation for the significant differences between previous unidirectional laboratory data and recent field measurements. If one considers a constant input-amplitude sum, equivalent to a constant crest probability level in a Gaussian analysis of a sea state, the introduction of even a small directional spread leads to a significant reduction in the nonlinear increase in the maximum local crest elevation. This reduction is difficult to predict in terms of the usual combination of free and bound waves, assuming that resonant or near-resonant effects take place very slowly (see Hasselmann 1962, 1963; Hammack & Henderson 1993).

In the unidirectional wave cases, it is clear that the nonlinear increase in the crest elevation cannot be explained by a constant free-wave regime, corresponding to the waves generated at the wave paddle, coupled with the development of associated bound waves in the vicinity of an extreme event. Indeed, the present results suggest that there is a local and rapid widening of the free-wave regime in the vicinity of the extreme. The local reduction in the trough–trough period, the change in the velocity of the largest crest, the shift in the focal position in both space and time, and the modification of the water-particle kinematics underlying the largest wave crest provide evidence of this effect. Furthermore, the present results suggest that it is this widening of the free-wave regime that is particularly sensitive to the directional spread. These results explain the large reduction in the nonlinear crest elevation, for a given input-amplitude sum, and hence the fact that directionally spread field data appear to be reasonably consistent with a weakly nonlinear second-order solution (Rozario *et al*. 1993).

Although important, these arguments only represent part of the overall picture. If, for a constant input-amplitude sum, directionally spread waves are less nonlinear, it follows that larger input amplitudes, and therefore larger crest elevations, may be produced prior to the onset of wave breaking. The present study has confirmed that this is indeed the case. More significantly, it has shown that for a given input frequency–amplitude spectrum, the wave components arising outside the initial input range at the limit of wave breaking are (relatively) independent of the directional spread. This seems to imply that some threshold corresponding to the breaking limit may be defined in terms of the energy redistribution to the higher frequencies. In intermediate and shallow water, the frequency-difference terms involving a transfer of energy to the lower frequencies (Longuet-Higgins & Stewart 1960) may be equally important. In a directionally spread sea, more linear input energy is required to achieve this threshold and consequently limiting waves in a directionally spread sea will be larger than unidirectional waves with the same frequency spectral bandwidth.

The present study has clearly highlighted the importance of the energy redistribution in the vicinity of a large wave event. This result has wider practical implications for the description of extreme ocean waves. In many design applications, crest elevations with return periods of 100 years or 10 000 years are commonly specified using the extremal statistics of a Gaussian wavefield. This approach is based upon the underlying frequency spectrum and therefore takes no account of local energy transfers. Indeed, the present mechanism provides a possible explanation for the occurrence of so-called 'freak' waves, or waves which lie outside the normal statistical predictions. Local kinematic predictions, based upon the commonly applied wave theories, will also be limited in terms of their ability to model these rapid energy transfers. Indeed, even the more sophisticated wave models (see, for example, the double Fourier series solution proposed by Baldock & Swan (1994)), which allow the waves to deform in both space and time, will be unable to reflect these important energy shifts.

This limitation is highly relevant to the calculation of the applied wave loading appropriate to the design of offshore structures. In particular, the description of very steep waves is believed to be critically important in the prediction of the nonlinear forces associated with the onset of dynamic response for fixed structures and the occurrence of wave slamming and green-water inundation for floating structures. Given the practical importance of such issues, the need for a directional wave model capable of describing the evolution of large short-crested waves is clear. Possible alternatives include (i) the application of modulation theory based on the nonlinear Schrödinger equation, although this would be limited to narrow-banded frequency spectra; and (ii) the development of new three-dimensional time-marching procedures capable of providing fully nonlinear calculations with no limitations on the frequency spectral bandwidth, but with a large computational cost. Irrespective of the method adopted, the present laboratory study has clearly highlighted the importance of directionality when seeking to define the characteristics of extreme (focused) transient surface water waves.

The present study formed part of the research programme 'Uncertainties in Loads on Offshore Structures' sponsored by EPSRC through MTD Ltd and jointly funded with Amoco (UK) Exploration Company, BP Exploration Operating Co Ltd, Brown & Root Ltd, Exxon Production Research Company, Health and Safety Executive, Norwegian Contractors a.s., Shell UK Exploration and Production, Den norske Stats Oljeselskap a.s. and Texaco Britain Ltd. The authors also gratefully acknowledge further funding from the Royal Norwegian Council for Scientific and Industrial Research.

References

Baldock, T. E. & Swan, C. 1994 Numerical calculations of large transient water waves. *Appl. Ocean Res.* **16**, 101–112.

Baldock, T. E., Swan, C. & Taylor, P. H. 1996 A laboratory study of nonlinear surface waves on water. *Phil. Trans. R. Soc. Lond.* A **354**, 649–676.

Belcher, S. E. & Vassilicos, J. C. 1997 Breaking waves and the equilibrium range of wind-wave spectra. *J. Fluid Mech.* **342**, 377–401.

Boccotti, P. 1983 Some new results on statistical properties of wind waves. *Appl. Ocean Res.* **5**, 134–140.

Dold, W. J. & Peregrine, D. H. 1984 Steep unsteady waves: an efficient computational scheme. In *Proc. 19th Int. Conf. Coastal Engineering (ASCE), Houston, TX*, vol. 1, pp. 955–967.

Dysthe, K. B. 1979 Note on the modification of the nonlinear Schrödinger equation for application to deep water waves. *Proc. R. Soc. Lond.* A **369**, 105–114.

Goda, Y. 1985 *Random seas and design of maritime structures.* Tokyo: Tokyo University Press.

Hammack, J. L. & Henderson, D. M. 1993 Resonant interactions among surface water waves. *Ann. Rev. Fluid Mech.* **25**, 55–97.

Hasselmann, K. 1962 On the nonlinear energy transfer in a gravity-wave spectrum, part 1. General theory. *J. Fluid Mech.* **12**, 481–500.

Hasselmann, K. 1963 On the nonlinear energy transfer in a gravity-wave spectrum, part 2. Conservation theorems, wave-particle anology, irreversibility. *J. Fluid Mech.* **15**, 273–281.

Henderson, K. L., Peregrine, D. H. & Dold, J. W. 1999 Unsteady water wave modulations: fully nonlinear solutions and comparison with the nonlinear Schrödinger equation. *Wave Motion* **29**, 341–361.

Johannessen, T. B. 1997 The effect of directionality on the nonlinear behaviour of extreme transient ocean waves. PhD thesis, Imperial College, University of London, UK.

Jonathan, P. & Taylor, P. H. 1995 Irregular, non-linear waves in a spread sea. In *14th Int. Conf. on Offshore Mechanics and Arctic Engineering (OMAE), Copenhagen, June 1995.*

Jonathan, P., Taylor, P. H. & Tromans, P. S. 1994 Storm waves in the northern North Sea. In *Proc. 7th Int. Conf. on the Behaviour of Offshore Structures, Cambridge, MA, USA*, vol. 2, pp. 481–494.

Lindgren, G. 1970 Some properties of a normal process near a local maximum. *Ann. Math. Stat.* **41**, 1870–1883.

Longuet-Higgins, M. S. 1952 On the statistical distribution of the heights of sea waves. *J. Marine Res.* **11**, 245–266.

Longuet-Higgins, M. S. 1974 Breaking waves in deep or shallow water. In *Proc. 10th Conf. on Naval Hydrodynamics, Cambridge, MA, USA*, pp. 597–605.

Longuet-Higgins, M. S. 1980 On the distribution of the heights of sea waves: some effects of nonlinearity and finite bandwith. *J. Geophys. Res.* **85**, 1519–1523.

Longuet-Higgins, M. S. 1987 The propagation of short surface wave on longer gravity waves. *J. Fluid Mech.* **177**, 293–306.

Longuet-Higgins, M. S. & Stewart, R. W. 1960 Changes in the form of short gravity waves on long waves and tidal currents. *J. Fluid Mech.* **8**, 565–583.

Miller, S. J., Shemdin, O. R.. & Longuet-Higgins, M. S. 1991 Laboratory measurements of the modulation of short wave slopes by long surface waves. *J. Fluid Mech.* **233**, 389–404.

Peregrine, D. H. 1983 Wave jumps and caustics in the propagation of finite amplitude waves. *J. Fluid Mech.* **136**, 435–452.

Peregrine, D. H., Skyner, D., Stiassnie, M. & Dodd, N. 1988 Nonlinear effects on focussed water waves. In *Proc. 21st Int. Conf. on Coastal Engineering (ASCE), Malaga, Spain*, vol. **1**, pp. 732–742.

Phillips, O. M. 1977 *Dynamics of the upper ocean.* Cambridge University Press.

Phillips, O. M. 1985 Spectral and statistical properties of the equilibrium range in wind-generated gravity waves. *J. Fluid Mech.* **156**, 505–531.

Phillips, O. M., Gu, D. & Walsh, E. J. 1993*a* Expected structure of extreme waves in a Gaussian sea, part 1. Theory and SWADE buoy measurements. *J. Phys. Ocean.* **23**, 992–1000.

Phillips, O. M., Gu, D. & Walsh, E. J. 1993*b* Expected structure of extreme waves in a Gaussian sea, part 2. SWADE scanning Radar Altimeter measurements. *J. Phys. Ocean.* **23**, 2297–2309.

Rapp, R. J. & Melville, W. K. 1990 Laboratory measurements of deep water breaking waves. *Phil. Trans. R. Soc. Lond.* A **331**, 735–800.

Roberts, A. J. 1983 Highly nonlinear short-crested water waves. *J. Fluid Mech.* **135**, 301–321.

Rozario, J. B., Tromans, P. S., Taylor, P. H. & Efthymiou, M. 1993 Comparisons of loads predicted using 'NewWave' and other wave models with measurements on the Tern structure. In *Wave kinematics and environmental forces*, vol. 29, Advances in Underwater Technology, Ocean Science and Offshore Engineering, pp. 143–158. Dordrecht: Kluwer.

Salter, S. H. 1984 Physical modelling of directional seas. In *Proc. Symp. Description and Modelling of Directional Seas, Technical University, Denmark*, paper B-1.

Sand, S. E., Ottesen Hansen, N. E., Klinting, P., Gudmestad, O. T. & Sterndorff, M. J. 1990 Freak wave kinematics. In *Water wave kinematics* (ed. A. Tørum & O. Gudmestad), pp. 535–549. Dordrecht: Kluwer.

Schaffer, A. M. 1993 Laboratory wave generation correct to second-order: wave kinematics and environmental forces. *Proc. Soc. Underwater Technol.* **29**, 115–139.

Sharma, J. N. & Dean, R. G. 1981 Second-order directional seas and associated wave forces. *Soc. Petroleum Eng. J.* **4**, 129–140.

Skyner, D. 1996 A comparison of numerical predictions and experimental measurements of the internal kinematics of a deep-water plunging wave. *J. Fluid Mech.* **315**, 51–64.

Stamnes, J. J., Løvhaugen, O. & Spjelkavik, B. 1983 Nonlinear focusing of surface waves by a lens—theory and experiment. *J. Fluid Mech.* **135**, 71–94.

Stansberg, C. T. 1991 Extreme wave asymmetry in full scale and model scale experimental wave trains. In *Proc. 10th Int. Conf. on Offshore Mechanics and Arctic Engineering (OMAE), Stavanger, Norway*, vol. 2, pp. 215–222.

Stansberg, C. T. 1994 Effects from directionality and spectral bandwidth on non-linear spatial modulations of deep-water surface gravity wave trains. In *Proc. 24th Int. Conf. on Coastal Engineering (ASCE), Kobe, Japan*, vol. 1, pp. 579–593.

Taylor, P. H. & Haagsma, I. J. 1994 Focusing of steep wave groups on deep water. In *Proc. Int. Symp. Waves—Physical and Numerical Modelling (IAHR), Vancouver, Canada*, vol. 2, pp. 862–870.

Tromans, P. S., Anaturk, A. & Hagemeijer, P. 1991 A new model for the kinematics of large ocean waves-application as a design wave. In *Proc. 1st Int. Offshore and Polar Engineering Conf., Edinburgh, UK*, vol. 3, pp. 64–71.

Whalin, R. W. 1972 Wave refraction theory in a convergence zone. In *Proc. 13th Int. Conf. on Coastal Engineering (ASCE), Vancouver, Canada*, vol. 1, pp. 451–470.